JOURNAL OF MATERIALS SCIENCE **37** (2002) 3337–3360

Adiabatic shear bands and examples of their role in severe plastic deformation

L. E. MURR, E. A. TRILLO, S. PAPPU, C. KENNEDY
Department of Metallurgical and Materials Engineering, University of Texas at El Paso, El Paso, TX 79968, USA

The accommodation of severe plastic deformation in impact crater formation, ballistic rod flow and penetration in thick targets, shaped charge formation, and a variety of friction-stir welding and processing is shown to occur by microstructure refinement, particularly dynamic recrystallization in the development of localized or overlapping adiabatic shear bands. Optical metallography and transmission electron microscopy observations of solid-state flow in adiabatic shear zones are compared to illustrate these mechanisms which can often involve intermixed microstructural regimes composed of recovery, recrystallization, and grain growth phenomena.

1. Introduction

Adiabatic shear, shear instabilities, and shear localization which manifest in adiabatic shear bands are known to occur in many extreme deformation or severe plastic deformation (SPD) applications [1]. These include impact cratering [2, 3] and penetration involving flow of both the penetrator and the target to form the penetration channel [4, 5], ballistic plugging [6], metalworking operations such as punching and machining [7], equal channel angular processing [1], and a variety of dynamic processing phenomena; including friction-stir welding and processing [8–10]. The shearing deformation actually achieved inside an adiabatic shear band is extremely large; with shear strains (γ) as large as 10 [11]. The mechanism to achieve this large strain involves dynamic recrystallization (DRX) and "superplastic" flow by sliding of the sub-micron, equiaxed, recrystallized grains. Dynamic recovery (DRV) and mechanically-assisted sub-grain (recovery microstructure) rotation and coalescence can also play a role in the evolution of equiaxed, recrystallized grains [12]. Shear bands generally nucleate at defects or defect saturated (fully strain-hardened or work-hardened) regions; or favorably oriented grains. Nucleation and growth of shear instabilities dictate the frequency and spacing of shear bands, and collective organization processes can create thick (or wide) regimes of, overlapping shear bands, where the regime will flow as a "fluid". Work hardening, strain-rate sensitivity, and thermal sensitivity play a key role in the flow or shear localization; with the adiabatic temperature rise (ΔT) within the shear band regime governed generally by the product of shear strain (γ) and shear-strain rate ($\dot{\gamma}$) ($\Delta T \propto \gamma\dot{\gamma}$). The resulting, localized thermal softening is therefore the main driver for shear band formation. Modeling and scaling laws have also been developed which describe the major aspects of adiabatic shear as outlined briefly in the foregoing narrative [13].

While quantitative descriptions of shear bands are generally lacking, there seems to be an emergence of microscopic observations of qualitative phenomena which provide, at least, a basic understanding of material flow in the solid-state. It is the intent of this paper to provide a broad overview of applications and areas where localized flow and shear band phenomena are observed, and to compare a wide range of shear band-related and residual flow phenomena using examples characteristic of very large strains, and high strain rates. These examples are drawn from studies of shaped charges, explosively-formed penetrators, impact craters, dense rod penetration of thick metal or alloy targets; as well as friction-stir welding and processing examples. In the case of penetrating rods, solid-state flow is associated with both the projectile and the target.

2. The onset of plastic deformation and its extension into the severe plastic deformation regime

Deformation, especially plastic or permanent, irreversible deformation, involves the generation of dislocations at instabilities in or on solids. In the case of perfect single crystals, such instabilities can only occur (ideally) at the surface (the solid/vapor interface). These instabilities are characterized by surface steps or ledges which create high strain or corresponding critical stress to create dislocations which propagate into the solid crystal by heterogeneous shear along crystallographic slip planes. In the case of more practical, polycrystalline solids these instabilities occur at internal interfaces or grain (or crystal) boundaries. However, dislocations can also be produced within the interfacial phase [14] and so-called extrinsic grain boundary dislocations often allow deformation to occur within the grain boundary regime before heterogeneous shear of

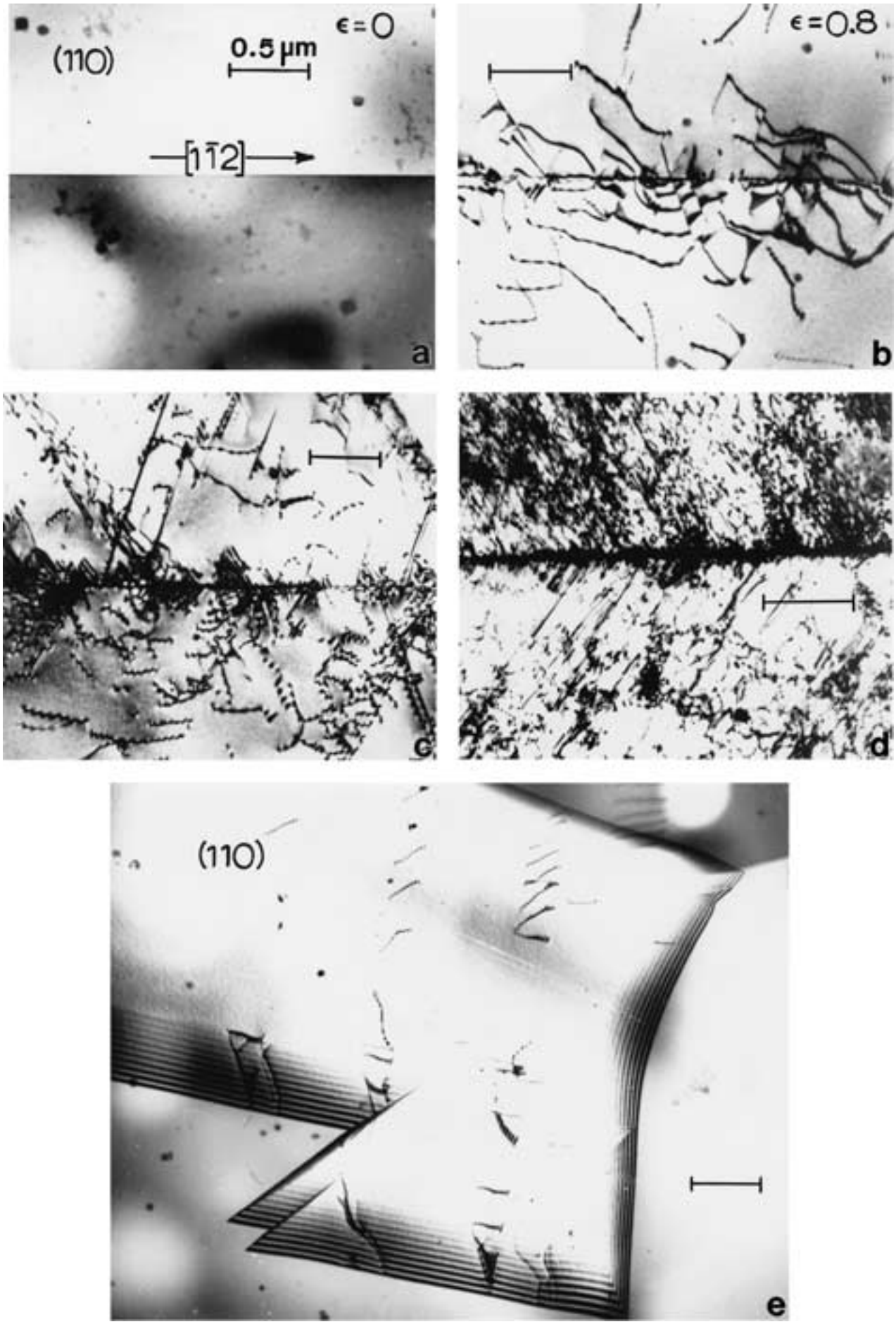

Figure 1 Thin foil (TEM) examples extracted from 304 stainless steel tensile specimens corresponding to strains noted. (a) to (e) are identical crystallographies and diffracting conditions noted in (a) ($\mathbf{g} = [1\bar{1}1]$). (a) $\varepsilon = 0$, (b) $\varepsilon = 0.8\%$, (c) $\varepsilon = 1.5\%$, (d) $\varepsilon = 12\%$, (e) $\varepsilon = 0.2\%$. Dislocation emission and pileup at grain boundaries. Magnifications are given in (a).

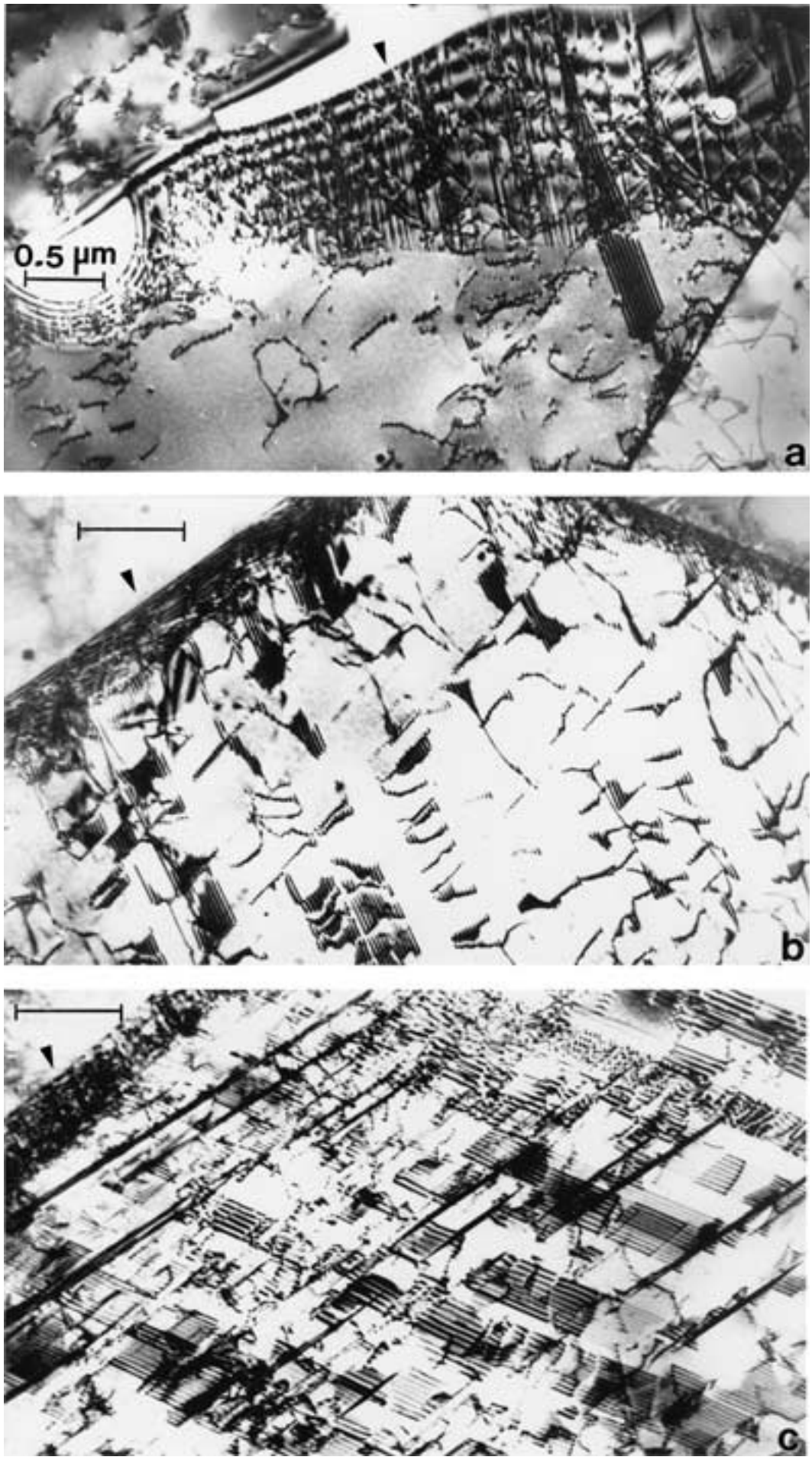

Figure 2 Continuation of thin foil (TEM) 304 stainless steel tensile specimens showing dislocation and related microstructure (ledge) variations at grain boundaries (arrows) corresponding to engineering strains noted. (a) $\varepsilon = 1.5\%$, (b) $\varepsilon = 2\%$, (c) $\varepsilon = 6\%$. Magnifications are indicated in (a). All matrix crystallographies and diffraction conditions are the same and as noted in Fig. 1a.

the boundary produces ledges or other critical sources for generating matrix (or regular crystal) dislocations. As a consequence, dislocations initially form preferentially at or near grain boundaries or other solid/solid interfaces and their density increases with increasing strain. These features are illustrated in Figs 1 and 2 for a common (type 304), austenitic (fcc) stainless steel.

Fig. 1 shows two important features. Fig. 1a to d shows the creation of dislocations at a coherent {111} twin boundary. This boundary has a specific crystallography which can serve as an unambiguous interfacial reference as a function of strain indicated. The trace direction of the boundaries is the same as indicated in Fig. 1a for a [110] zone. The operating reflection is also a common ⟨111⟩ reflection creating the dislocation contrast in Fig. 1a to d. Consequently the dislocation density is unambiguously represented as a function of engineering strains noted. The other important feature noted in Fig. 1e is that at an engineering strain of 0.2%, every grain exhibits dislocations emitted from one or more boundaries enclosing the grain. But more importantly, dislocations are observed to propagate from one boundary to the other. Consequently there is no dislocation source within the grain and dislocations emerge from ledges created as instabilities within the interface. There are no so-called Frank-Read sources within the grains. Fig. 2 expands these observations and demonstrates that as dislocations are created from grain boundary sources and propagate into the crystal grains, the grain boundaries also illustrate very high densities of dislocations and complex dislocation structures.

The examples in Figs 1 and 2 are particularly pertinent since the stacking-fault free energy is relatively low (~25 mJ/m^2) [14], and dislocations within the crystal grains occur along uninterrupted, linear {111} arrays. For metals of high stacking-fault free energy such as nickel ($\gamma_{SF} \sim 128$ mJ/m^2) or aluminum ($\gamma_{SF} \sim 160$ mJ/m^2; estimated at room temperature) [14], extensive cross-slip will not allow dislocation propagation to be viewed with any confidence at low strains in the initial plastic deformation regime. Dislocation sources are the same in these metals and originate at the grain boundaries. Interactions can occur sooner by cross-slip and dislocation multiplication within the grains may occur somewhat sooner in high stacking-fault free energy materials, but the multiplication mechanisms will ultimately be essentially the same [14–16]. The rate of multiplication, etc. will be characteristic of so-called work-hardening or strain-hardening and at higher strains the grains themselves will become deformed or distorted (Fig. 2). Severe grain deformation will also require dislocation slip or shear within the interfacial phase [14], which also reaches some limit or saturation similar to the crystal matrix. At some critical strain, the internal or plastic strain energy saturates and recovery and recrystallization occur either allowing for large shear through special interfacial orientations, or extensive grain refinement which facilitates large shear strains by grain sliding. These instabilities arising to accommodate severe plastic deformation occur as variations in shear bands composed of recovered, oriented, and/or recrystallized grains. Fig. 3 shows a simple engineering stress-strain diagram representing these plastic deformation regimes.

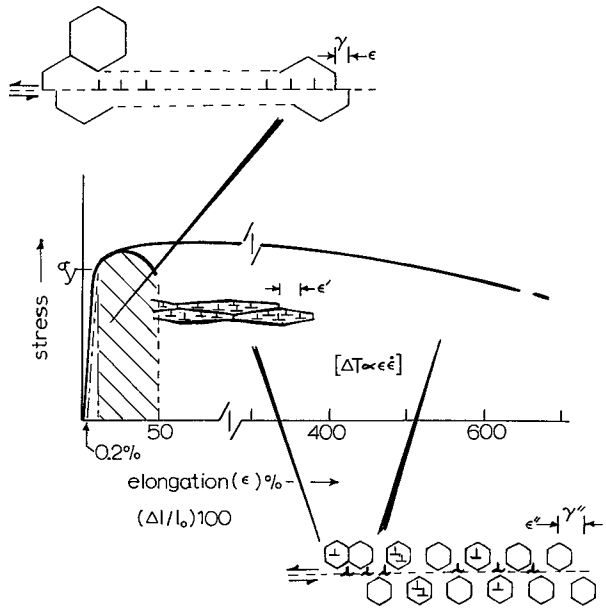

Figure 3 Schematic for extended engineering stress-strain diagram. Deformation regimes are illustrated schematically to involve dislocation emission (at grain boundary ledges) and slip (⊥) corresponding to strains ε, grain deformation corresponding to strains ε', and grain refinement and (extrinsic) grain boundary dislocation glide (⊥) (or superplastic flow) corresponding to strains ε''. Corresponding shear strains are denoted γ, while the actual, extended plastic deformation may be considered superplastic, the residual material is not necessarily superplastic.

The schematic representation in Fig. 3 for the extreme shear accommodated by adiabatic shear bands (and the like) by recrystallization and grain refinement shows special grain boundary dislocation slip accommodating the shear or superplastic flow. While grain boundary (GB) shearing or sliding is usually thought to account for superplastic flow, the actual extent of shear measured along the boundaries (indicated by γ'' in Fig. 3) is only about 1/3 of the total shear strain. Consequently, the other 2/3 of the strain must come from the deformation of the grains. Li [17] has recently proposed a new mechanism for severe plastic (or superplastic) deformation involving an "interfacial fluid" layer (or regime) as the source of the plasticity; a concept characteristic of the schematic illustration in Fig. 3. This interfacial layer (or phase [14]) can, according to Li [17], be sheared and "squeezed" to produce compressive (or tensile) strain. Plastic flow is continuous because the "interfacial fluid" is essentially inexhaustible.

Fig. 4 shows an impact crater cross-section in a copper target as an example of the full range of deformation and plastic phenomena illustrated schematically in the extended stress-strain diagram of Fig. 3. The crater bottom or wall is composed of a roughy 50 μm thick dynamic recrystallization (DRX) zone which allows material to flow out of the crater region to form the rim, which stretches outward, and particulates to eject flowing material from the crater in the solid state. Below this solid-state flow regime there is a band of heavily deformed and distorted polycrystalline material. This is highly work-hardened and increases in hardness as indicated in the corresponding microhardness profile.

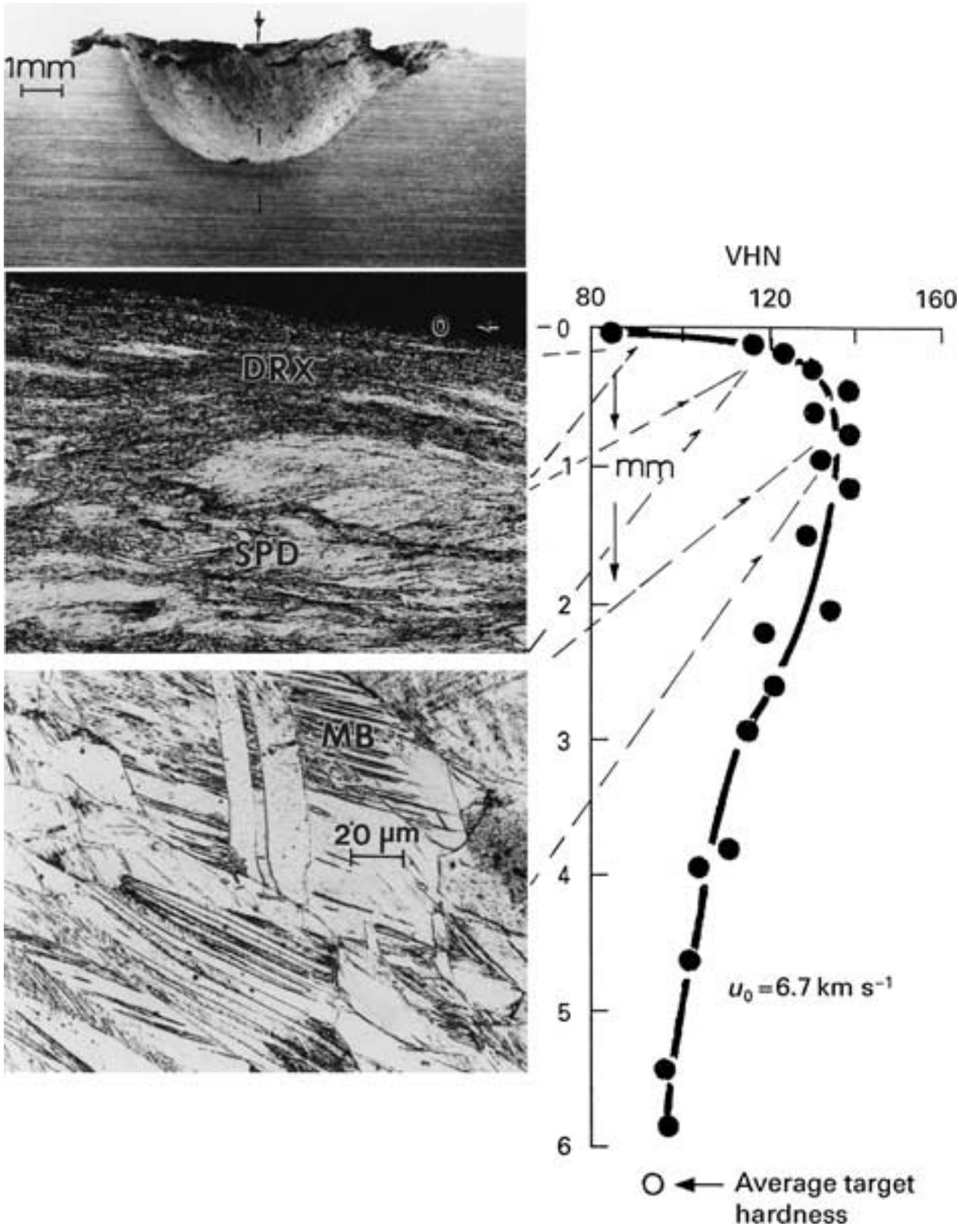

Figure 4 Hypervelocity aluminum projectile impact crater formation in a copper target (a); showing residual microstructure evolution (b); and corresponding microhardness profile extending along the impact axis from the crater bottom (c). Microstructure zones in (b) are denoted DRX, SPD (characterized by highly deformed grains as in Fig. 3) and MB (microband zone).

There is a wide zone of relatively undistorted grains containing a high density of microbands which decline in density into the target as the hardness declines. Dislocation cells occur beyond the microband zone and their size increases to the base target dislocation cell size where the hardness is the same as the base target hardness.

3. Adiabatic shear bands and penetrator/penetration flow

While Fig. 4 illustrates how the extended stress-strain diagram and the specific implications of Fig. 3 can be applied in the accommodation of the extreme deformation implicit in solid-state flow during crater formation, similar phenomena accommodate the deformation and

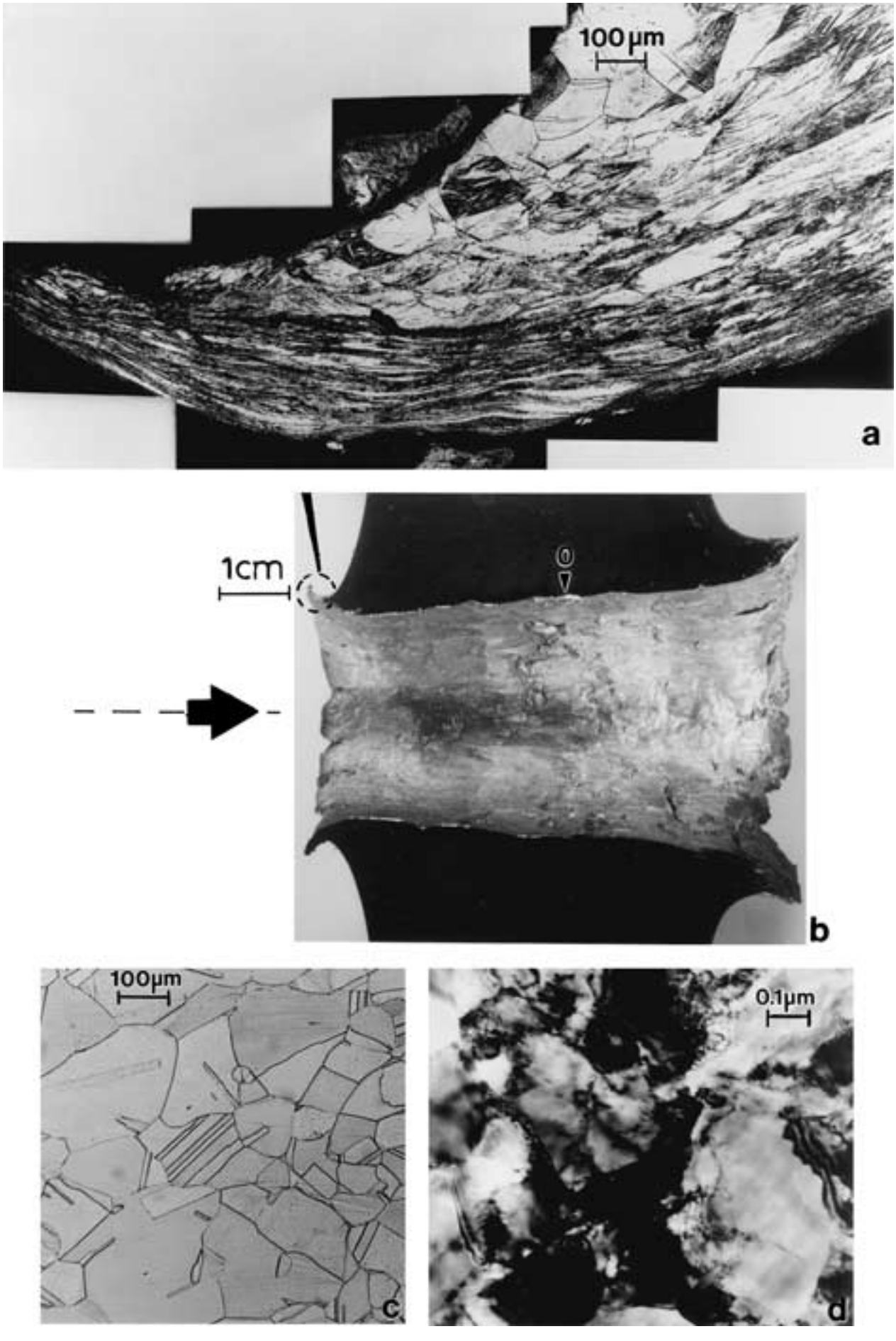

Figure 5 Thick copper target penetration by 0.78 cm diameter WHA rod (1.5 km/s). (a) Crater rim flow features magnified from (b) as noted by arrow. The large arrow in (b) denotes the impact direction and effective penetrator diameter. (c) Base target grain structure. (d) TEM image of recrystallized grain structure in the crater wall region and characteristic of the shear band regime in (a).

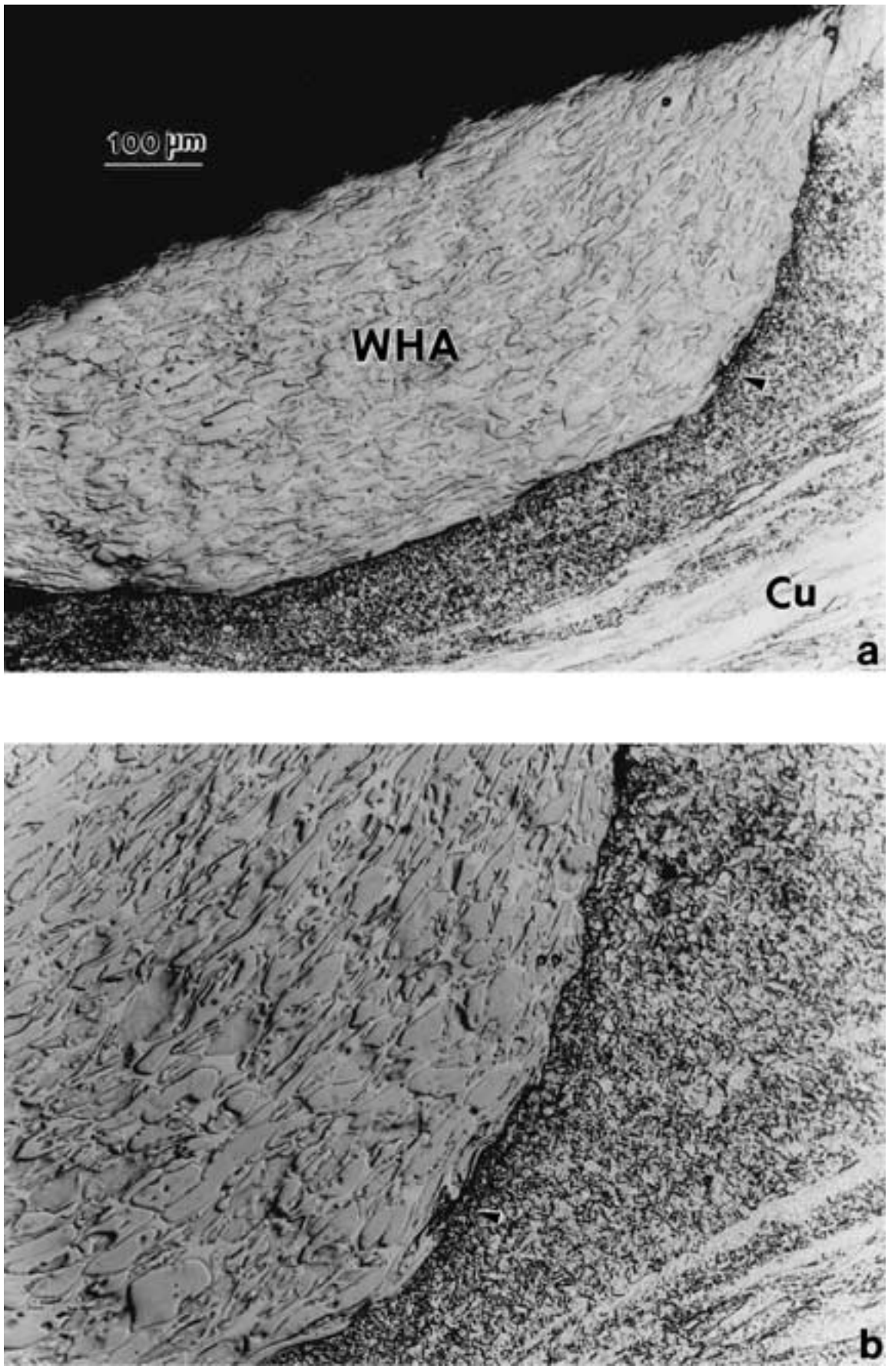

Figure 6 WHA penetrator rod erosion product embedded in DRX zone along penetration channel in Fig. 5b (a). (b) shows enlarged view at reference arrow in (a).

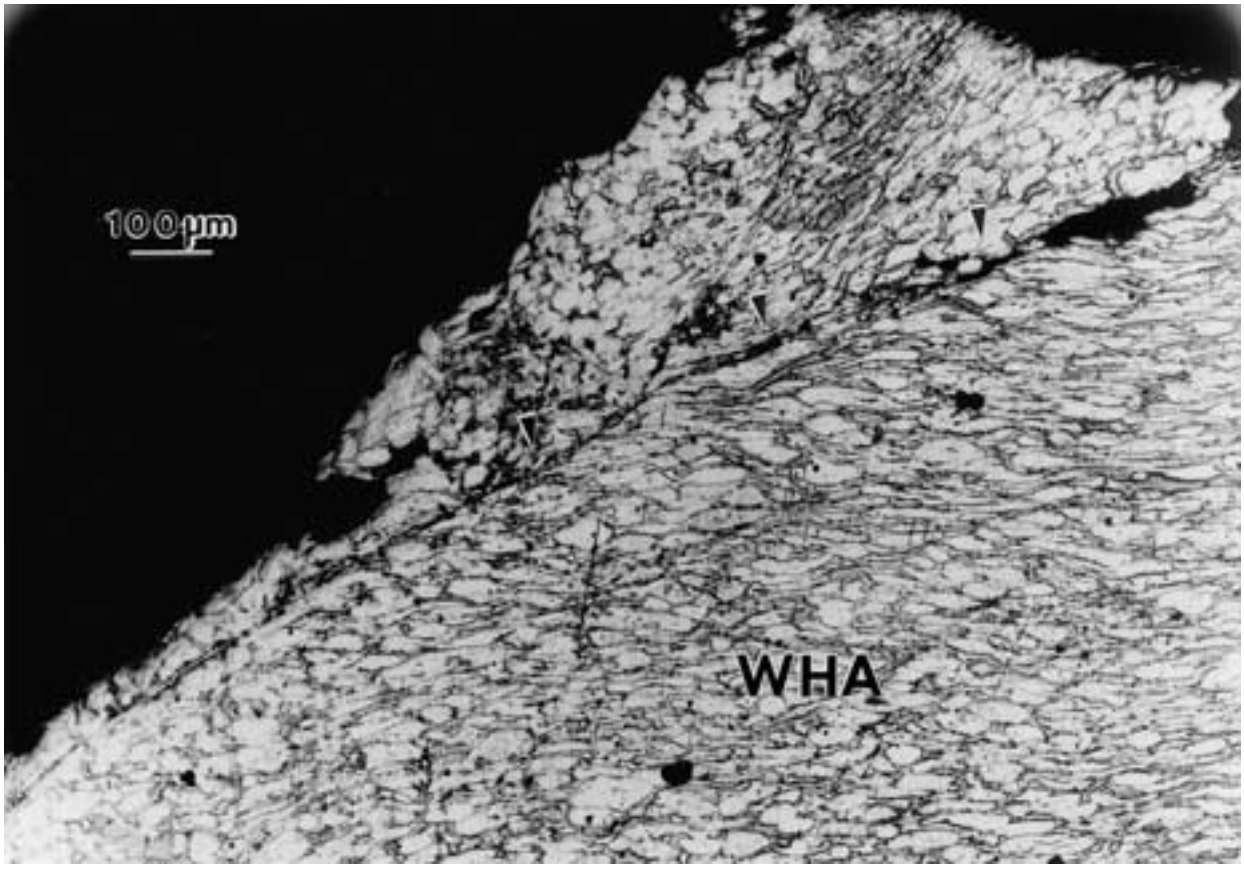

Figure 7 Shear band (arrows) in WHA erosion product as in Fig. 6.

flow of both the penetrator and the target in ballistic perforation. These features are illustrated in the series of micrographs, photographs, and associated microhardness data reproduced in Figs 5 to 10 for the perforation of thick copper and aluminum 7039 targets by tungsten heavy-alloy (WHA : 93% W, 5% Fe, 2% Ni) rods impacting at 1.5 km/s. In Fig. 5 the WHA rod (penetrating in the direction noted by the large arrow in Fig. 5b) causes target material to flow in opposition to that direction. The Cu target flow occurs by a region of overlapping shear bands composed of DRX grains as shown by the enlarged rim cross-section (Fig. 5a). The penetration channel wall therefore consists of a layer of DRX-refined grains as in Fig. 4, and shown in contrast to the target base in Fig. 5c and d.

Figs 6 and 7 show eroded WHA rod fragments embedded in the penetration channel wall in Fig. 5. Fig. 6b shows an enlarged view of the WHA particle in Fig. 6a and the large DRX zone in which it has flowed. In Fig. 7, the eroded WHA particle exhibits classical adiabatic shear bands (ASB) as noted by the arrows.

Figs 8 and 9 show penetration in strain-hardened and very hard aluminum 7039 as compared with the copper target penetration in Fig. 5. The most prominent feature is the very narrow penetration channel in the aluminum-alloy target in contrast to the copper target, and in contrast to the actual penetrator diameter. It is also apparent that the aluminum alloy target contains a propensity of cracks at the back or exit surface, and the slightly magnified views in Fig. 8b and c illustrate somewhat regularly spaced and bifurcated ASB's. These ASB's often intersect overlapping flow regimes also composed of DRX-refined grains along the penetration channel wall as illustrated in Fig. 9. The DRX zone along the penetration channel wall in Fig. 8 is considerably smaller than that along the wall in Fig. 5, and gives rise to the much more restricted flow in the aluminum alloy target. The full hard aluminum target does not allow for deformation energy storage beyond the penetration channel and the channel does not expand into the target. This restriction creates periodic shear instabilities and cracking during penetration. In effect, the strain energy of deformation is invested in ASB and crack formation in the fully-hardened aluminum alloy since no additional deformation can be accommodated by the target itself. This feature is illustrated in Fig. 10 which compares the typical residual hardness profiles for the copper target in Fig. 5 and the 7039 aluminum target in Fig. 8. The aluminum alloy exhibits a saturated hardness in contrast to the copper.

Fig. 11 shows the formation of adiabatic shear bands in WHA penetrators in rolled homogeneous armor (RHA) steel; and extends the features illustrated for WHA erosion fragments shown in Fig. 7 above. The interesting feature of the sintered WHA rods (Fig. 11a) is the roughly spherical nature of the W particles which can act like intrinsic circular strain gauges (Fig. 11b), approximating biaxial strains in deformed cross-sections (Fig. 11c–e). Fig. 11c illustrates the accommodation of very large deformations through the shear flow of penetrator blocks along the ASB's (arrows). Fig. 11d and e show W particle deformation associated with ASB's and other heavily deformed regions of the WHA penetrator rod. The details of the W

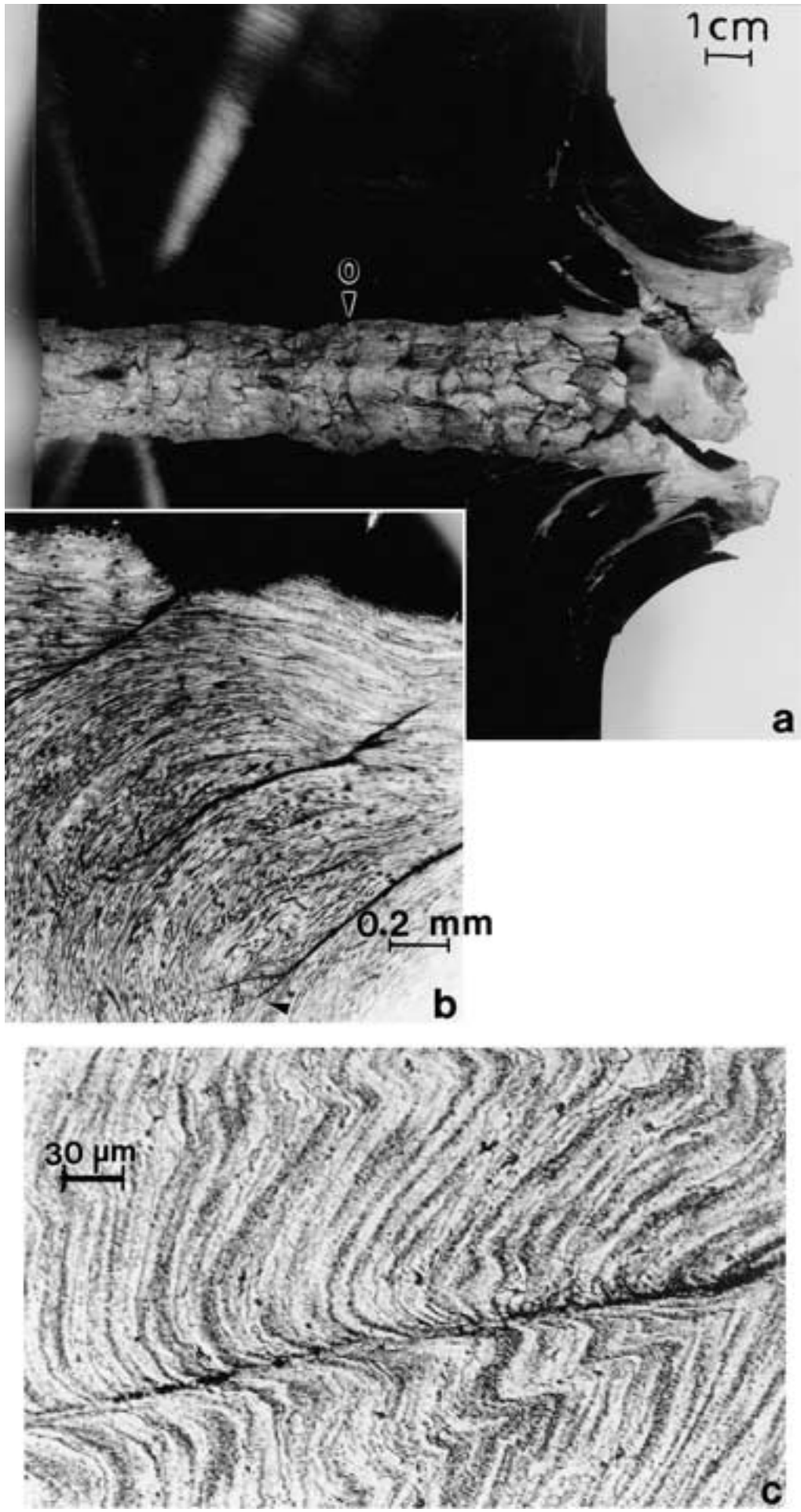

Figure 8 Thick aluminum 7039 target penetration by 0.78 cm diameter WHA rod (1.5 km/s) (a) penetration channel half section. (b) Shear bands and flow features along penetration channel wall in (a). (c) Shear band enlargement at arrow in (b).

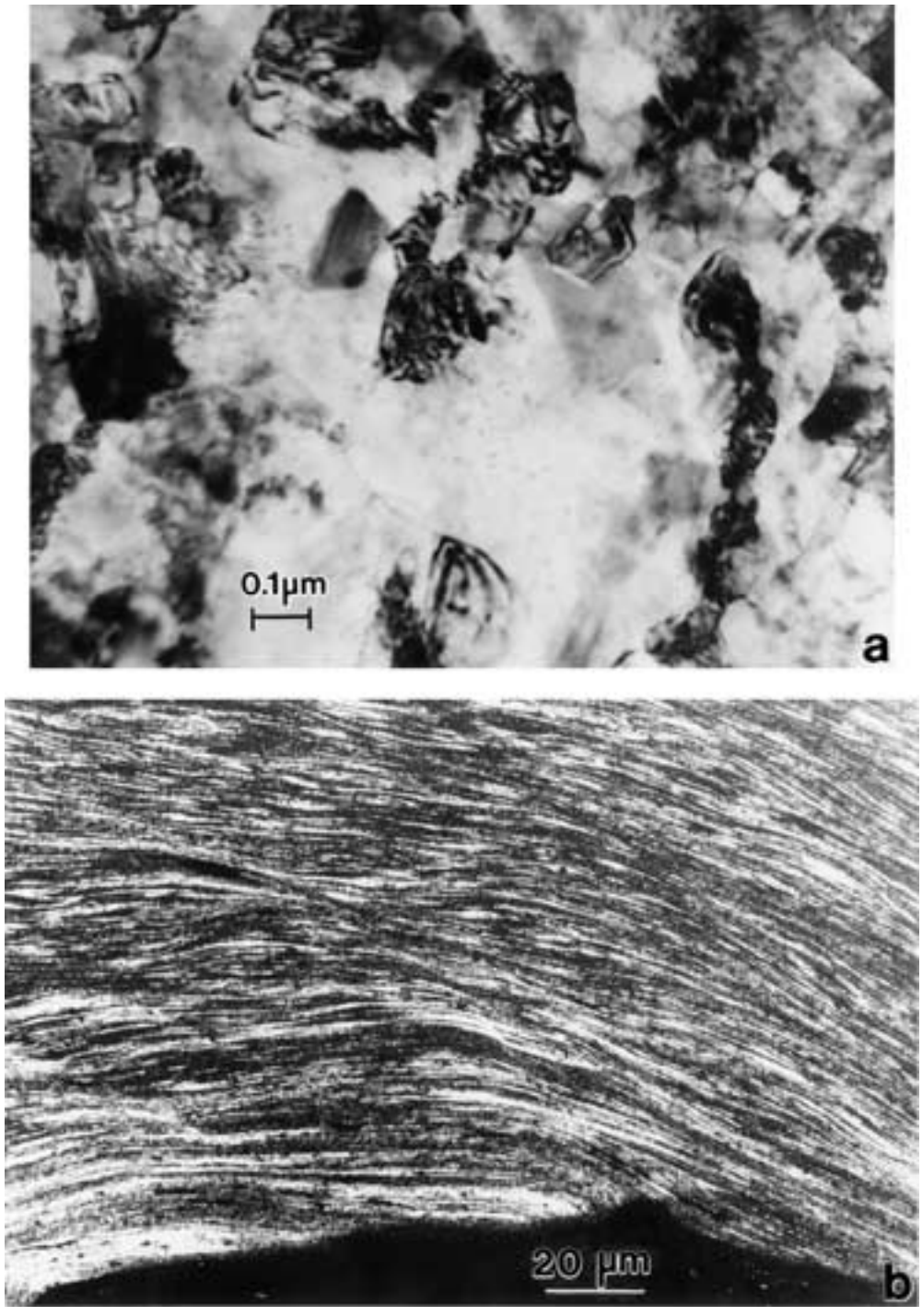

Figure 9 (a) Recrystallized, equiaxed grain structure typical of narrow flow regime (b) next to penetration channel wall in Fig. 8a.

particle microtructures are compared in Fig. 12 for the initial W particles in the undeformed rod of Fig. 11b (Fig. 12a) and a deformed region such as the right-hand portion of Fig. 11d (Fig. 12b).

Figs 13 to 15 represent comparisons of tungsten and tungsten-alloy (4% Ta) single-crystal rods, which have penetrated RHA steel (MIL-A-12560, class 3 steel), with the WHA penetrated rods in Fig. 11. Fig. 13a shows a [001] oriented W penetrator rod in RHA. Eroded rod material has flowed along the penetration channel and there are heavy flow features at the mushroomed head of the rod which are essentially the same as those features illustrated for the crater rim formation and target flow shown in Fig. 5a. These features are shown in more detail in the enlarged views in Fig. 13b

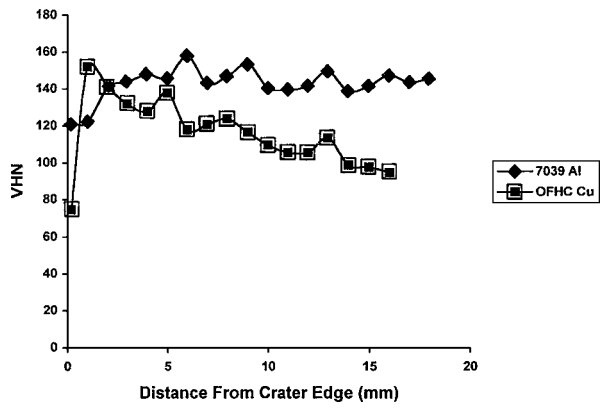

Figure 10 Residual microhardness profiles referenced to the penetration channel wall at (0) in Figs 5b and 8a (data from [4]).

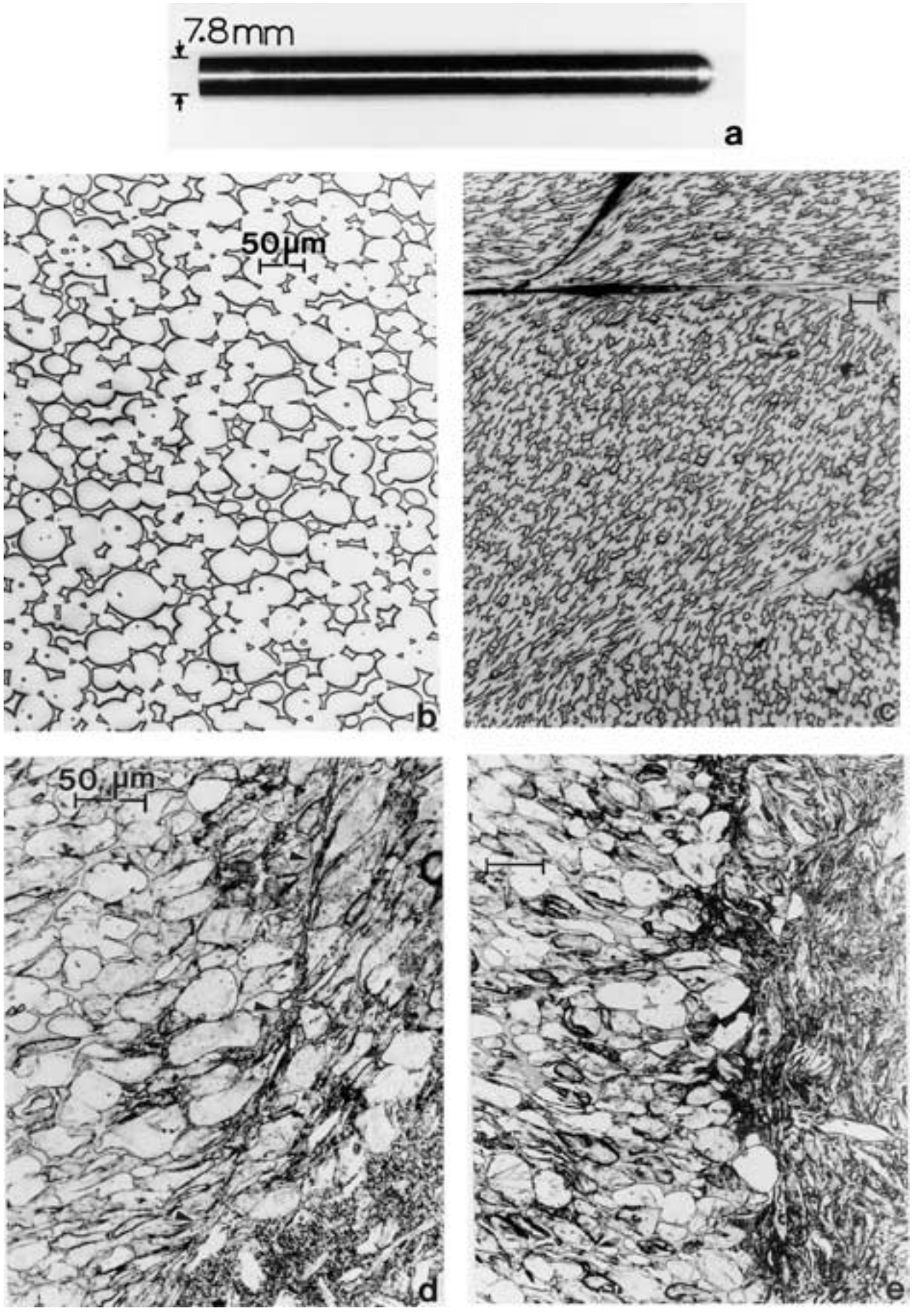

Figure 11 Deformation of WHA rod(a). (b) Shows the original rod cross-section microstructure consisting of W particles (nearly spherical) in a Ni-Fe matrix. (c) Head section of WHA penetrator in RHA target. (1.5 km/s impact velocity). (d) Shear band (arrows) and deformation of WHA penetrator rod. (e) Deformed WHA region to right.

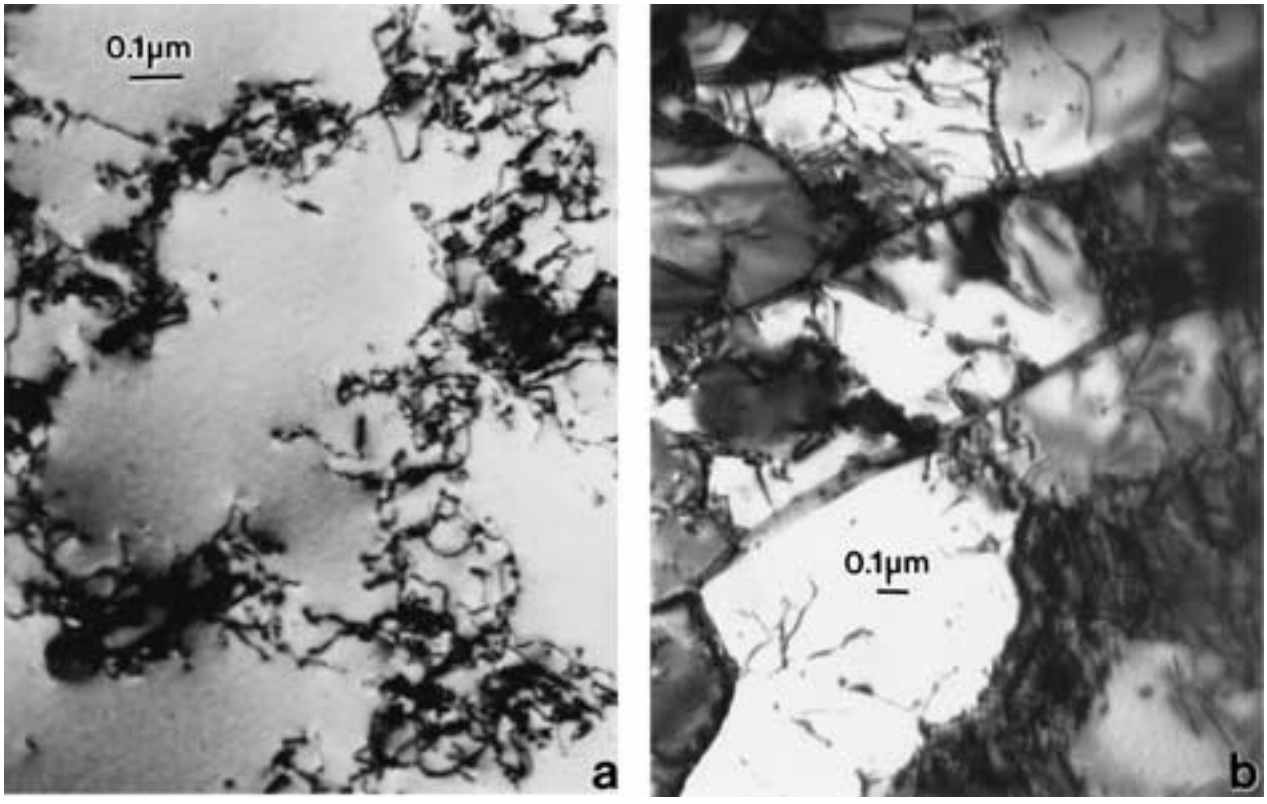

Figure 12 TEM images of W particle interior in original WHA rod (a) and deformed rod as in Fig. 11e (b). (a) Shows loose dislocation cells while (b) shows dislocation and sub-grain structures.

and c. In Fig. 13b, deformation twins observable at D in Fig. 13a, at the rear of the eroded projectile, are observed to bend into the shear bands and to be effectively accommodated by them, i.e., precursors in forming DRX grain structures. These features are illustrated in Fig. 13c which shows a large, DRX zone near the central portion of the flow zone at the mushroomed head in Fig. 13a. Fig. 14 compares the axial microstructures for the initial [001] W rod and a section within the mushroomed head in Fig. 13a. The microstructure in Fig. 14b, supported by the corresponding selected-area electron diffraction (SAED) pattern, illustrates the DRX grain refinement which characterizes the overlapping shear bands responsible for the rod flow on penetrating the RHA target. Especially notable in the SAED pattern of Fig. 14b are the large misorientations ($>12^{\circ}$) characterizing the equiaxed DRX grain structure.

Fig. 15 shows a flow regime at the head of a W-4% Ta [001] single-crystal rod embedded in an RHA target exhibiting flow phenomena similar to Fig. 13. A large DRX zone similar to that shown in Fig. 13c is shown in Fig. 15c.

The differences in penetrating rod deformation and flow illustrated on comparing Figs 11, 13, and 15 are similar to those exhibited on comparing target deformation and flow in Figs 5 and 8. Those differences are recognized as wide ASB zones accommodating continuous, homogeneous plastic flow in contrast to narrow, heterogeneous ASB zones (or classical ASB's) accommodating discontinuous movements of blocks, and even the fragmentation of deformed penetrators and targets.

4. Recovery and recrystallization accommodating severe plastic deformation in shaped charges

In the extension of shaped charge jets to strains or elongations in excess of 600 per cent, there are no classical ASB zones observed in recovered jet fragment microstructures. The entire jet fragment cross-section is usually completely recrystallized, and in addition, there is apparent grain growth. In contrast to the recovered jet fragments, the larger, shaped charge slug exhibits a continuous microstructure change throughout the recovered cross-section. These features are illustrated generally in the series of micrographs and photographs shown in Figs 16 to 18 for tantalum.

Fig. 16b shows a recovered tantalum jet fragment while Fig. 16d shows a cross-section view consisting of fairly uniform, equiaxed, DRX grains; and some grain growth. Fig. 17 illustrates a schematic evaluation of the jet formation and particulation as well as a comparison of the starting liner microstructure (Fig. 17a and b) and a recovered jet microstructure (Fig. 17d). Fig. 16e shows a corresponding, recovered, shaped-charge slug (Fig. 16a) while Fig. 16c shows a cross-section view consisting of a range of microstructures symmetrically disposed from the outer surface to the slug center. These are illustrated in Fig. 18. In Fig. 18a near the outer slug edge (corresponding to (a) in Fig. 16c), elongated dislocation cells and microbands dominate while midway to the slug center recovery and recrystallization are intermixed as shown in Fig. 18b. The slug center consists of equiaxed, recrystallized grains as shown in Fig. 18c.

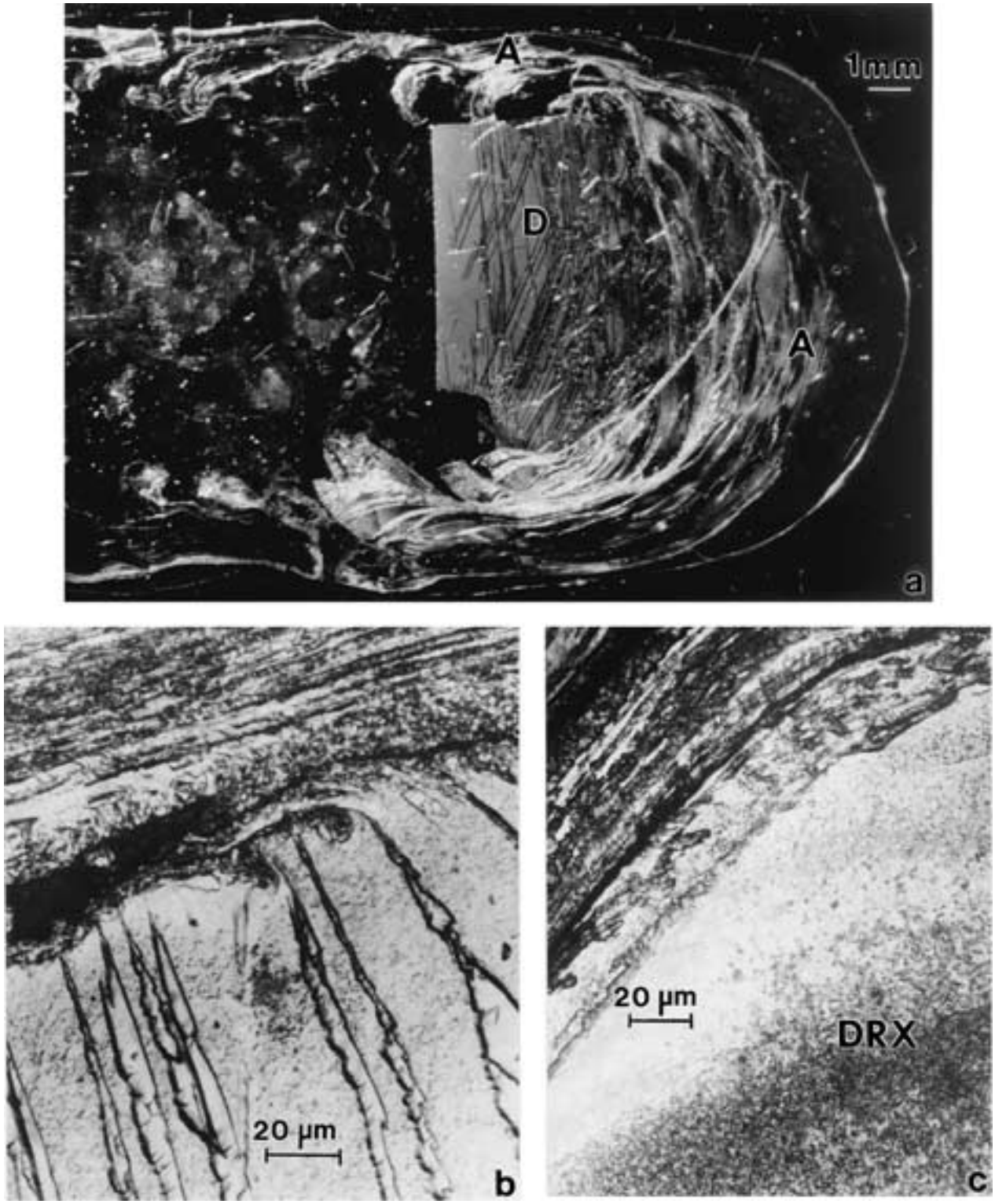

Figure 13 [001] W rod in RHA target (1.5 km/s impact velocity). (a) Flow features in head of projectile are noted in region A. E denotes erosion products flowing from projectile head. Deformation twins are observed at D. (b) Deformation twins bending into flow zone characterized by DRX bands. (c) Flow zone composed of overlapping shear bands and large DRX zone near projectile head in (a).

The schematic shown in Fig. 17c can be observed to be a variation of the extended stress-strain diagram shown in Fig. 3. The grain deformation and recrystallization could, depending upon the melting temperature and strain rate, be a continuous process. That is, recrystallization could occur more than once during the stretching of the jet to particulation. At the time of particulation only grain growth could occur. There is in fact a difference between the equiaxed grain size in the recovered jet fragment in Fig. 16d in contrast to the equiaxed grain structure at the center of the recovered slug (Fig. 16e). Compare Fig. 17d and Fig. 18c.

5. Adiabatic shear structures and DRX in friction-stir welding and processing

Figs 19 to 22 illustrate a range of adiabatic shear band and DRX examples for friction-stir welded (FSW) and

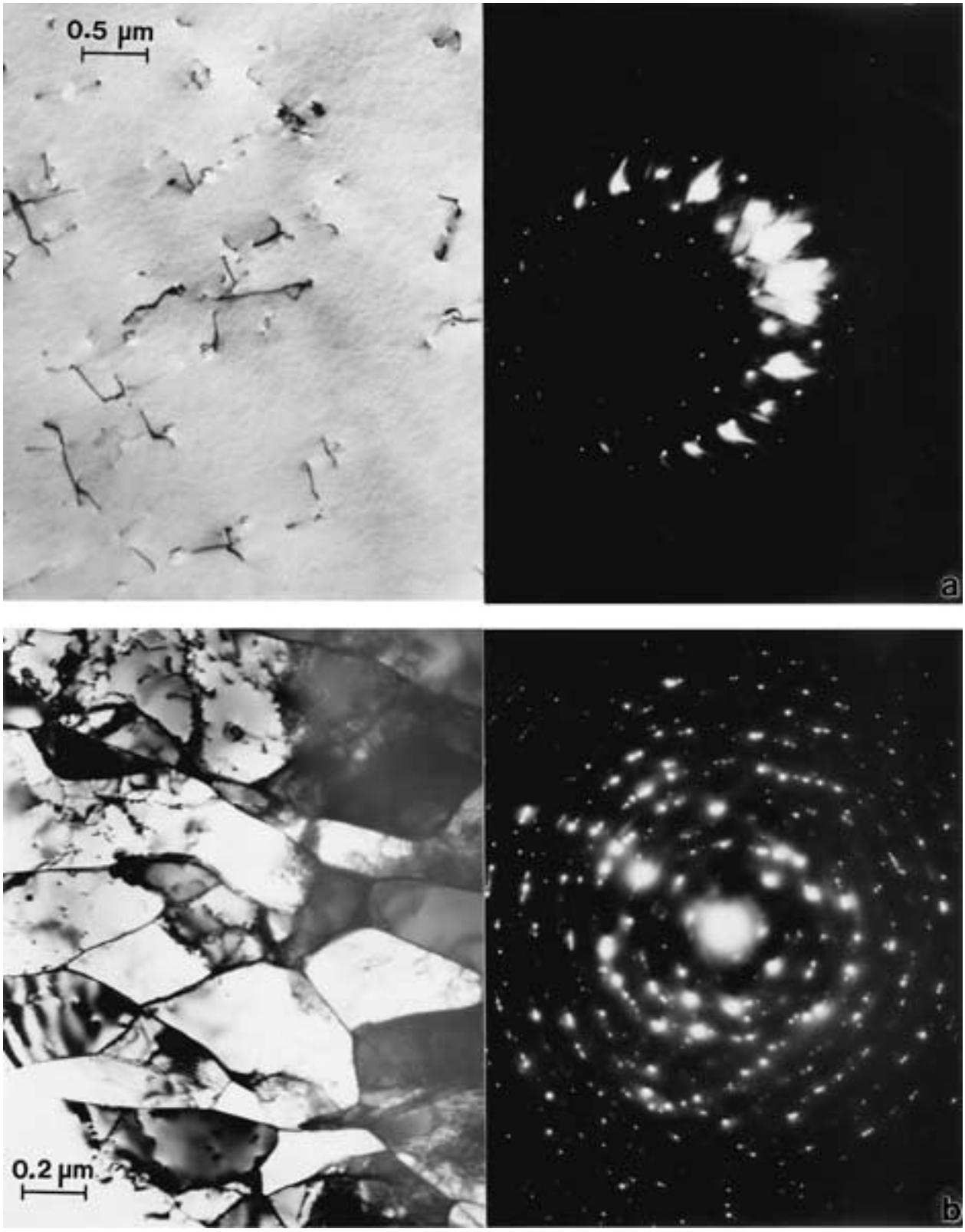

Figure 14 TEM images of initial [001] W rod microstructure (a) and typical microstructure in flow zone (A) in penetrator head in Fig. 13a. (b) Corresponding SAED pattern in (a) shows [001] orientation while in (b) the pattern shows a wide range of misorientations characteristic of the recrystallized zone.

processed (FSP) metals and alloys. Fig. 19 provides a range of schematic views of the solid-state, SPD which characterizes the stir-related flow. The physical nature of FSW or FSP is illustrated schematically in Fig. 19a while the formation of shear zones characterized by DRX and grain growth are illustrated in Fig. 19b to e. Fig. 19b is essentially synonymous with the microstructural evolution depicted in Fig. 3 for the extended stress-strain diagram. Fig. 19c and d show intercalation bands on shear zones created by DRX of two different materials (illustrated by butting different materials A and B in Fig. 19a). Fig. 19d is indicative

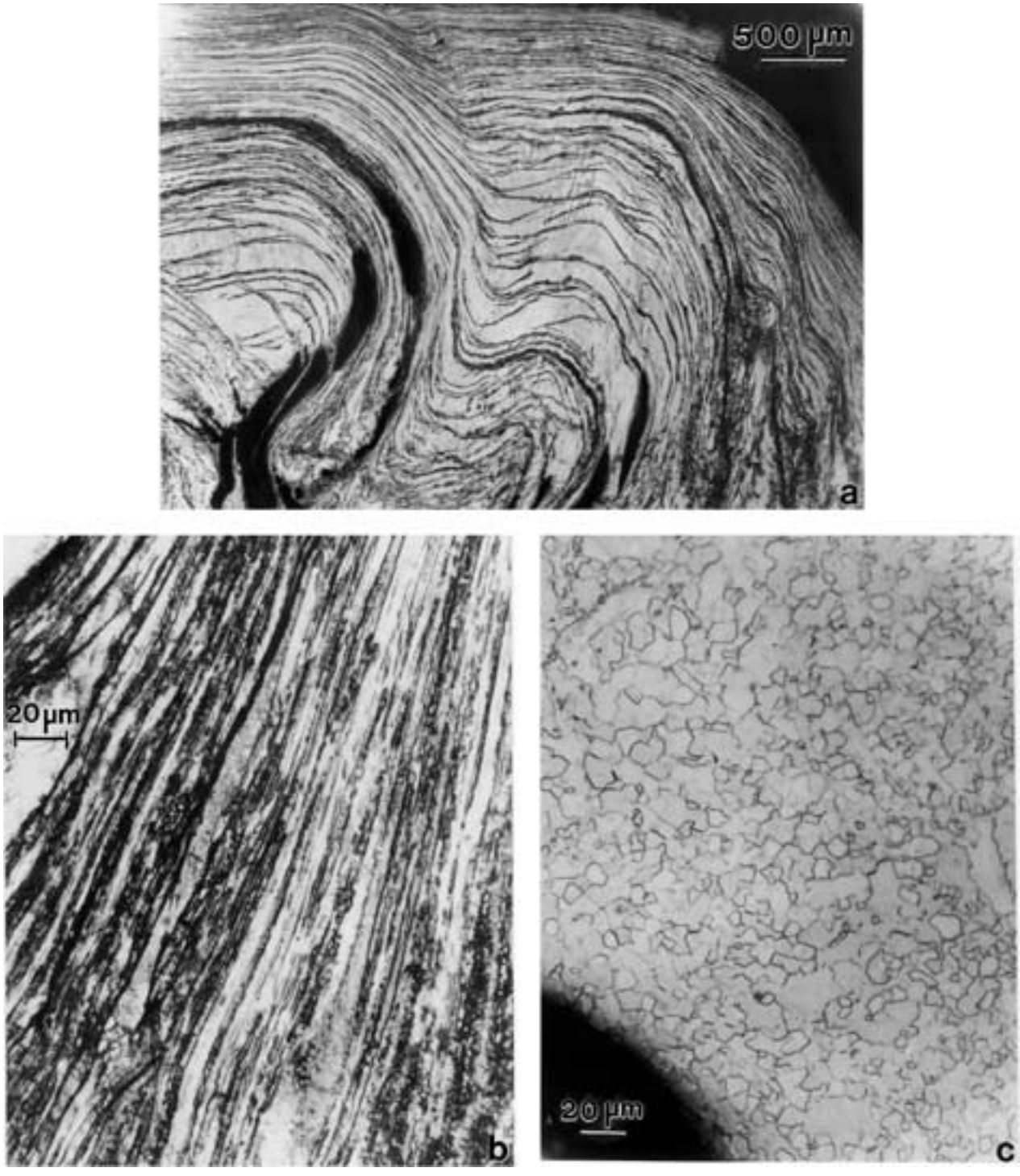

Figure 15 Flow features characteristic of a section of the head of a [001] W-4% Ta penetrator in RHA. (a) Overlapping shear band features. (b) enlarged view of (a) showing recrystallized grain structures. (c) DRX zone in central portion of the projectile head in (a).

of a difference in the DRX or grain growth of one of the different metals while Fig. 19e is indicative of an essentially primitive or minimal shear band composed of two DRX layers which glide to transport large blocks of material similar to the movement of target or penetrator blocks as illustrated above in Figs 8c and 11b respectively.

Fig. 20 illustrates typical, complex, fluid-like flow patterns characteristic of the schematic features illustrated in Fig. 19; especially the intercalation flow patterns for dissimilar metals FSW. All of the whorl, swirl, and vortex structures noted in Fig. 20 and characterized by DRX and grain growth phenomena have been well documented by both optical metallography and TEM [9, 18–20]. Fig. 21 shows examples of solid-state flow of large solids in DRX, fluid-like regimes. In Fig. 21a and b, particulated Cu segments from a 0.2 mm Cu insert between the A and B plates in Fig. 19a are observed to flow around the pin tool in an aluminum 6061 alloy after FSW. Fig. 21c and d show the similarities in homogeneous distributions of SiC particles in an aluminum A339 cast metal-matrix composite (MMC) containing 20 volume per cent SiC in the base metal cross-section, and in the FSW zone

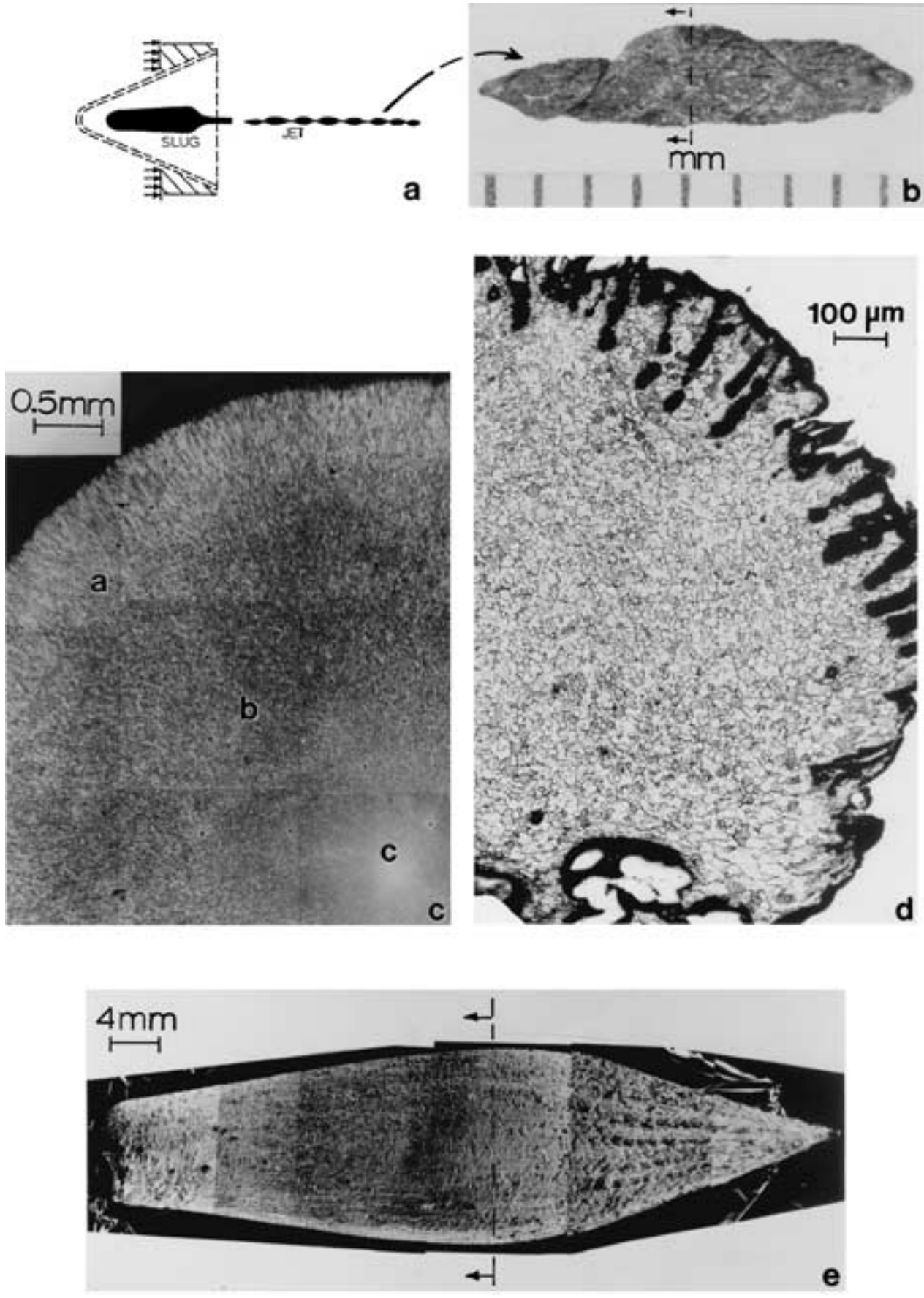

Figure 16 Tantalum shaped charge components and microstructures. (a) Shaped charge schematic. (b) Recovered jet fragment. (c) Slug cross-section (arrows in (e)). (d) Jet cross-section (arrows in (b)). (e) Recovered slug.

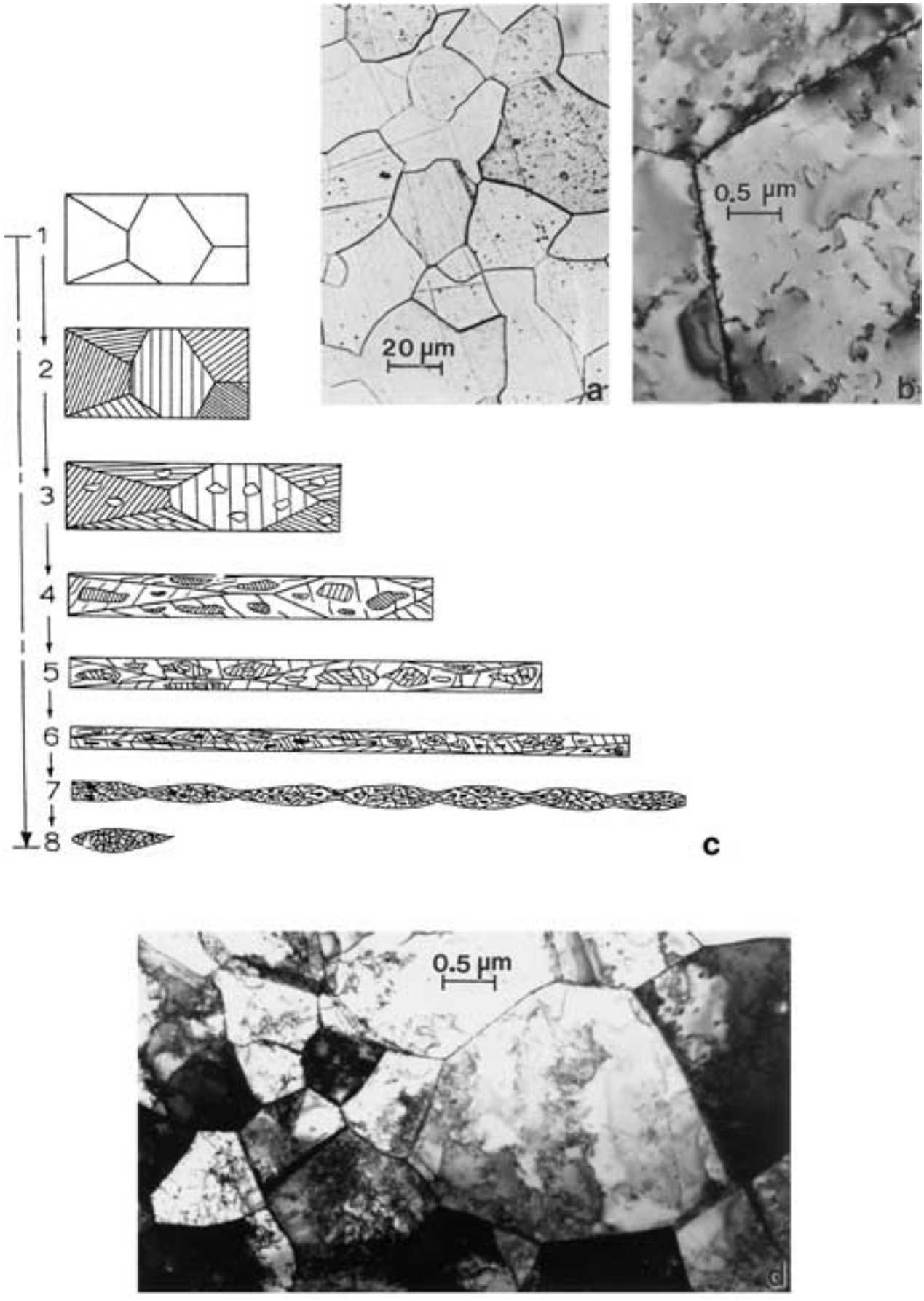

Figure 17 Evolution of tantalum shaped charge jet microstructure (a) and (b) show optical and TEM images of grain structure in the original Ta shaped charge cone (Fig. 16(a)). (c) Shows a schematic of DRX evolution. (d) TEM image of DRX grains in a recovered jet fragment as in Fig. 16d.

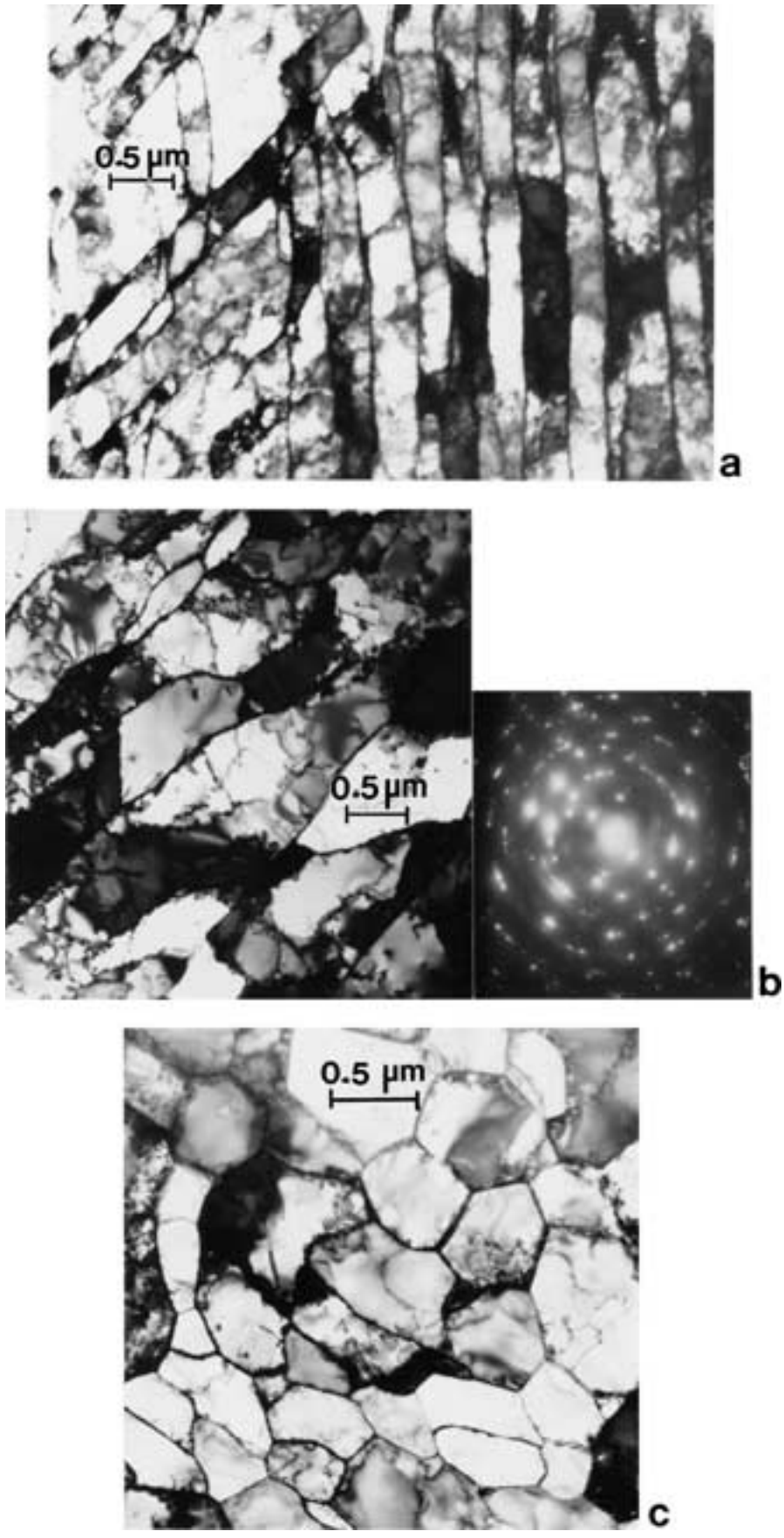

Figure 18 Variation of residual microstructures composing Ta slug cross-section as shown in Fig. 16c. (a) Shows microbands (b) shows recovery microstructures. Note range of misorientation in corresponding SAED pattern. (c) Equiaxed DRX grain structure at slug center.

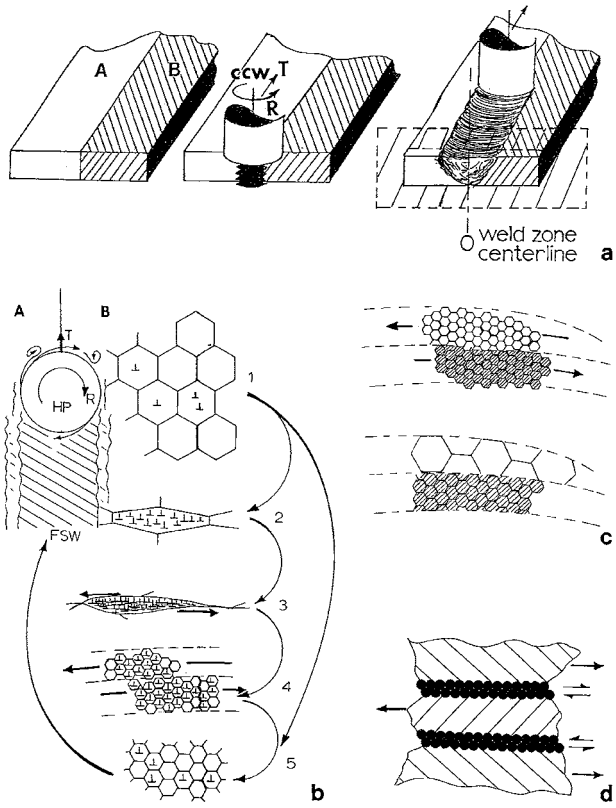

Figure 19 Friction-stir welding and processing schematics. (a) FSW process features a rotating tool which traverses the seam of butted plats A and B. (b) Shows a cartoon illustrating solid-state material flow by DRX during FSW. (c) Shows two sliding shear bands of different materials (d) shows grain growth of one shear zone. (e) Shows simple adiabatic shear bands allowing shear movement of solid material blocks.

center as a consequence of flow in the DRX regime created.

Fig. 22 shows the intermixing of beryllium and aluminum equiaxed grains (Fig. 22d) as a consequence of the FSP of a 62% Be-38% Al composite alloy created by a powder metallurgy route, and illustrated in Fig. 22a. In the FSP regime illustrated in Fig. 22, the reprocessed Be-Al alloy within the weld zone (Fig. 22d) increased in residual hardness by roughly 40% in contrast to the base metal hardness characteristic of the as-processed material illustrated in the microstructure view of Fig. 22a.

6. Discussion and summary

We have demonstrated, in retrospect, a range of examples involving severe plastic deformation (involving high strain and high strain rates—$\sim 10^3$ to 10^6 s^{-1}); and illustrating extreme plastic flow in the solid state to involve DRX either in a narrow, adiabatic shear band or a nearly continuous zone of wide, overlapping shear bands. We designate the recrystallized, generally equiaxed grain regimes as DRX zones but implicit in the accommodating microstructures are complex interplays between recovery and recrystallization microstructures as well as grain growth. Consequently, there are regimes such as in FSW where recovery, recrystallization, and grain growth can occur in a complex and even simultaneous fashion.

We have illustrated in Figs 14b and 18b rather classically that large misorientation angles ($>12^\circ$) are

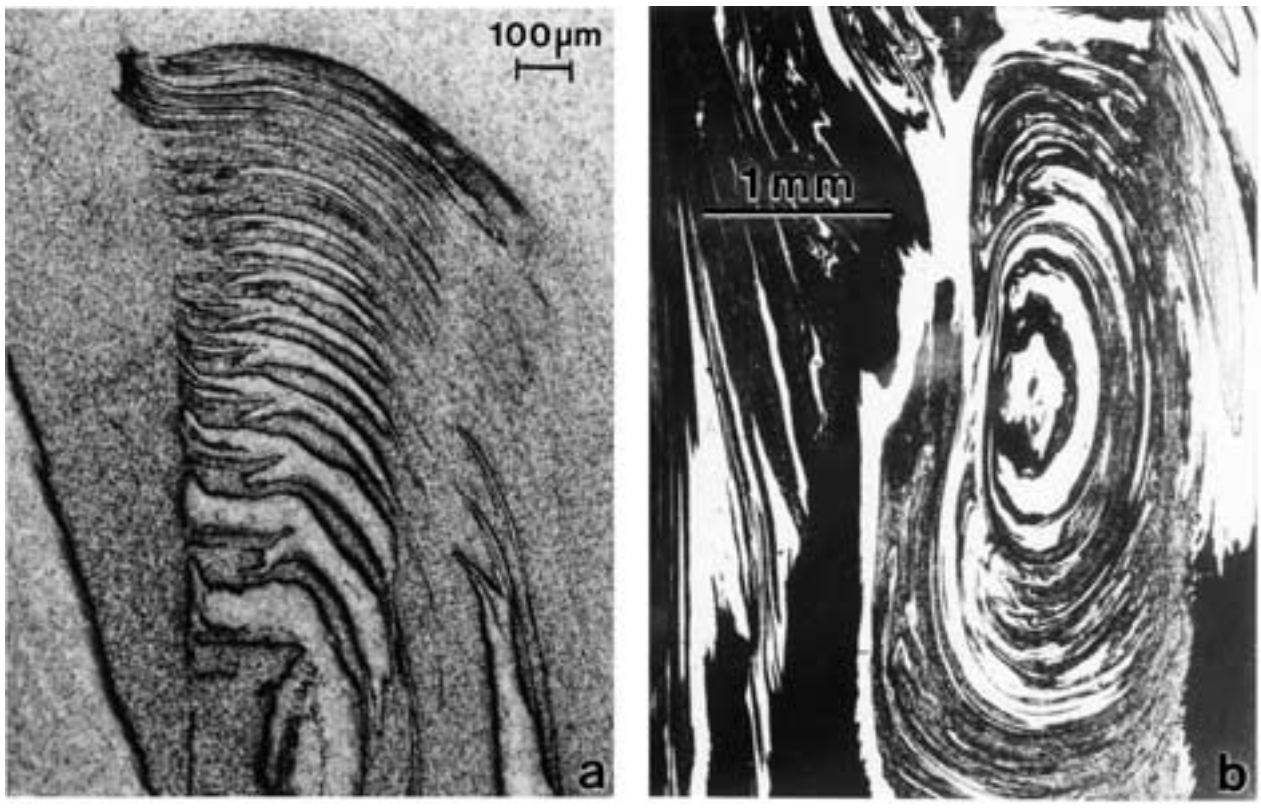

Figure 20 Examples of residual, complex flow features following FSW. (a) Cu blocks and shear features in the DRX brass zone of FSW of Cu and brass (70 Cu 30 Zn). (b) Complex flow patterns for FSW of 7050 Al and 7075 Al. (c) Complex flow zone in Cu/Al FSW. (d) Complex flow showing intercalation of Ag and brass shear structures in FSW of Ag/brass. (*Continued*.)

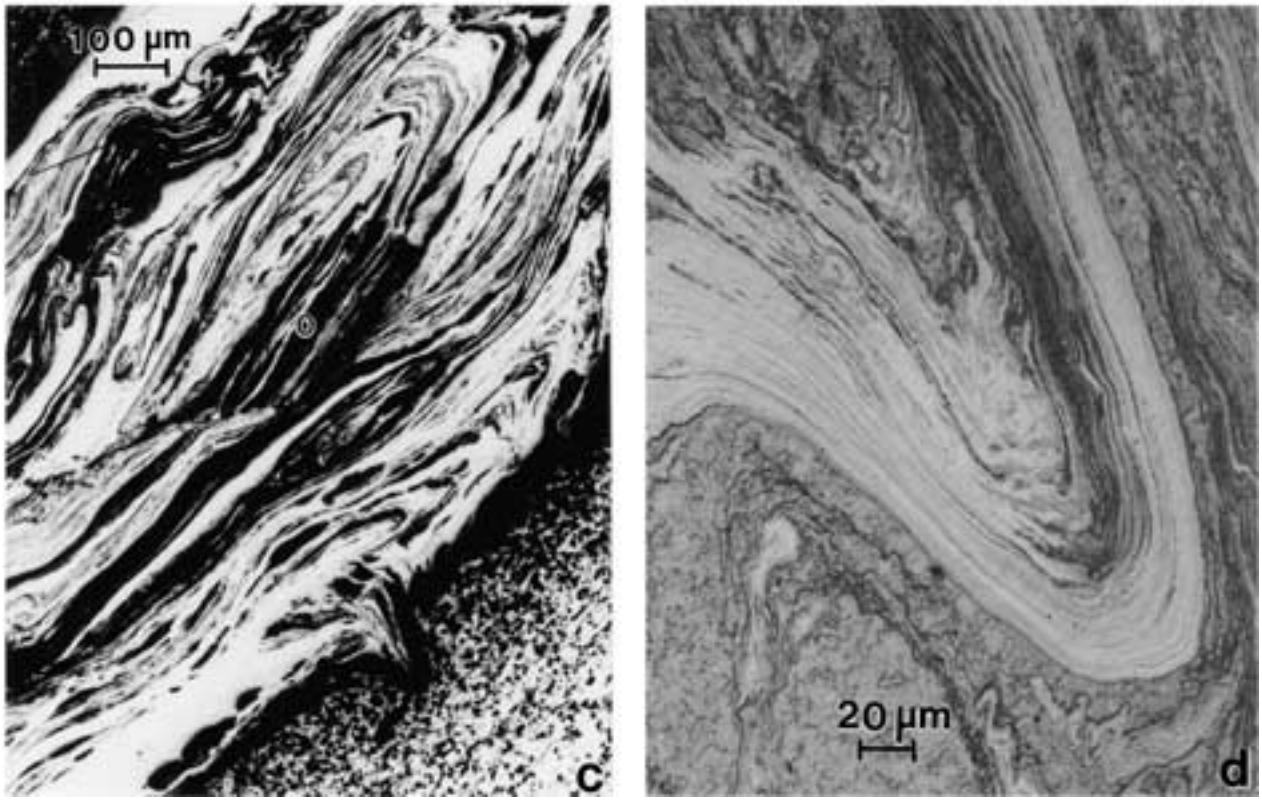

Figure 20 (*Continued.*)

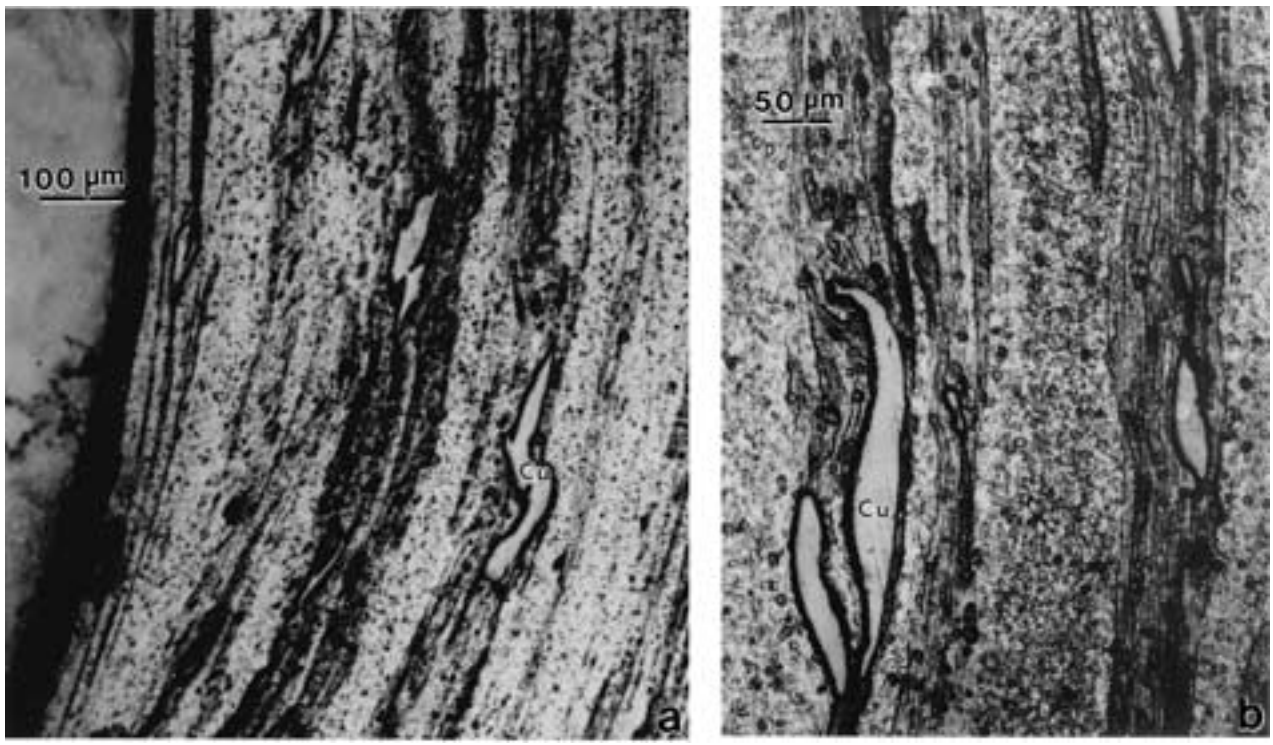

Figure 21 Examples of solid blocks of material flowing in the DRX flow zone during FSW. (a) and (b) show examples of Cu particles flowing in aluminum 6061 shear band zone. (c) Aluminum A339 containing 20% SiC particles. (d) FSW zone following welding of (c). Note similar distribution of the SiC particles in (c) and (d). (*Continued.*)

involved in characterizing the DRX or refined microstructures, and Figs 13c, 14b, 15c, 16d and 22d among others show the generally equiaxed, residual grain structures. However, the notion that recrystallization usually involves the development of high-angle (or high-energy) boundaries is a fundamentally false premise since it is contrary to the second law of thermodynamics. The preferred, recrystallized microstructures would consist of low-angle interfaces; with a preference for elongated structures where the maximum

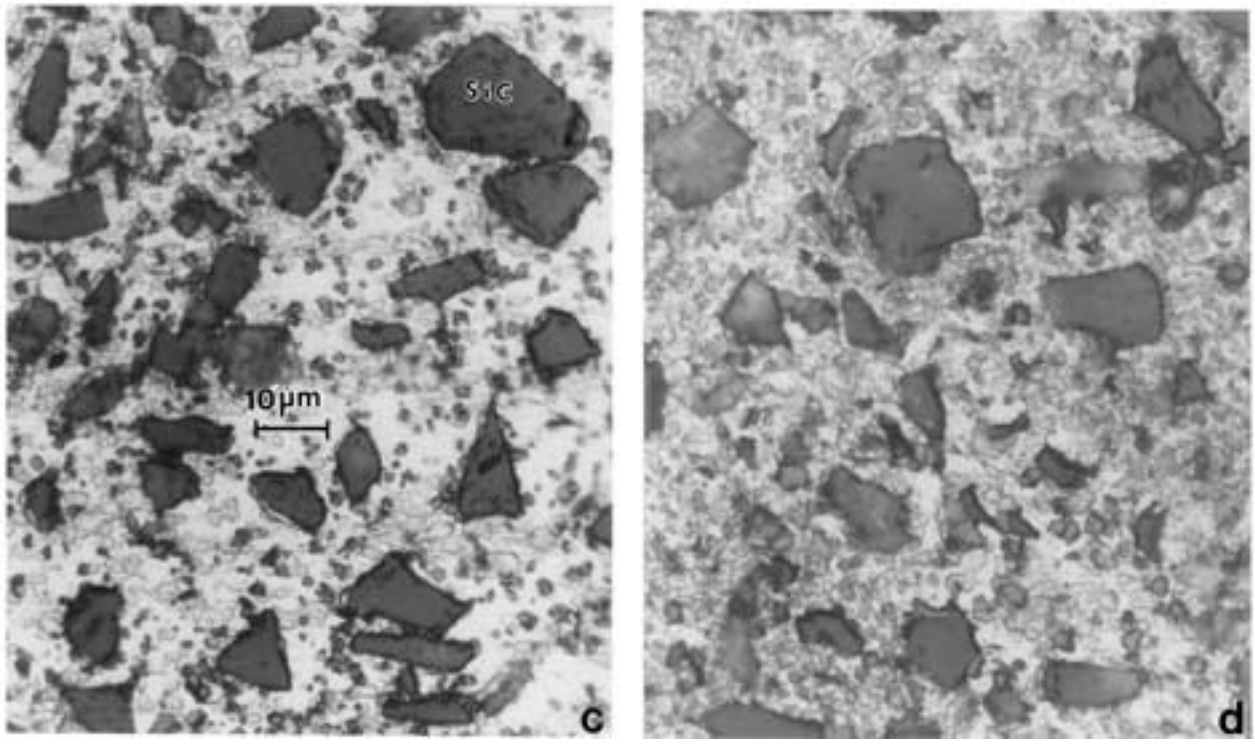

Figure 21 (*Continued.*)

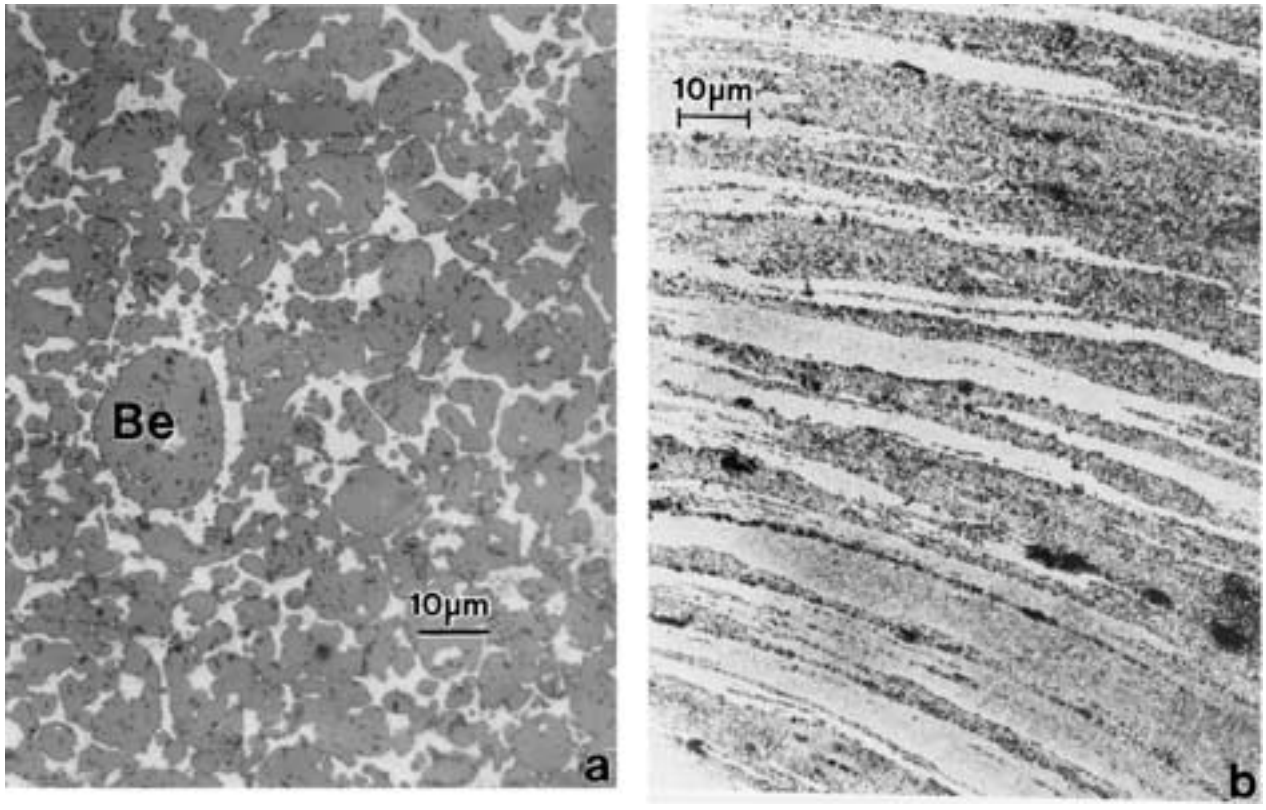

Figure 22 Friction-stir processing of Be 62-Al 38 MMC. (a) Original alloy showing Be particles in Al matrix. (b) Friction-stir processed zone showing DRX refired shear bands. (c) TEM image of (a). (d) TEM image of (b) showing intermixing of DRX Be and Al grains. (*Continued.*)

number of boundaries have been eliminated. These elongated, low-energy structures may possess crystallographic coincidence which facilitates shear or gliding on the interface, or in the interfacial regime. While very small, equiaxed grain structures may facilitate solid-state flow, there will be a simultaneous tendency for grain coalescence and grain growth, especially when adiabatic heating occurs during deformation-induced flow; and the internal microstructure is driven by the second low. It is therefore not unexpected that residual, recrystallized grain structures will exhibit very small misorientations or mixtures of misorientations as higher-energy (or higher angle) boundaries or microstructures are refined, possibly by torques or other

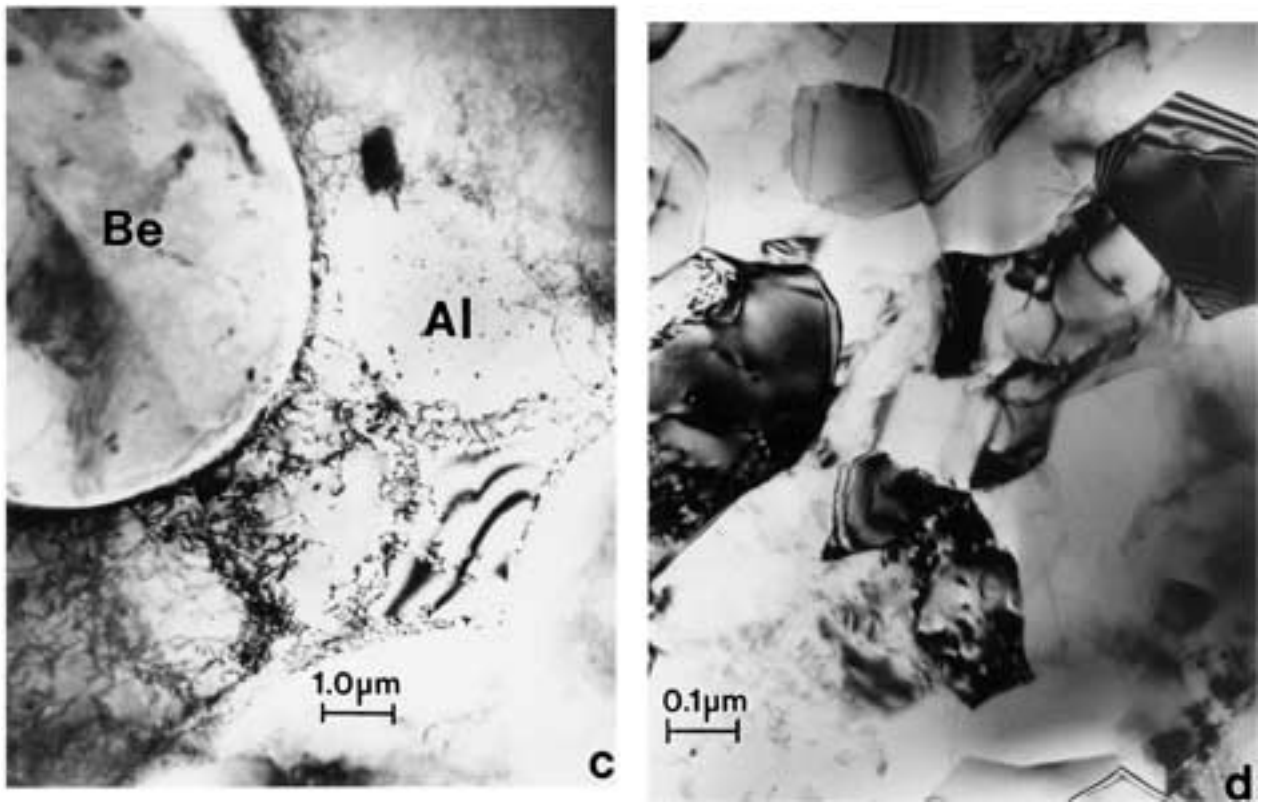

Figure 22 (*Continued.*)

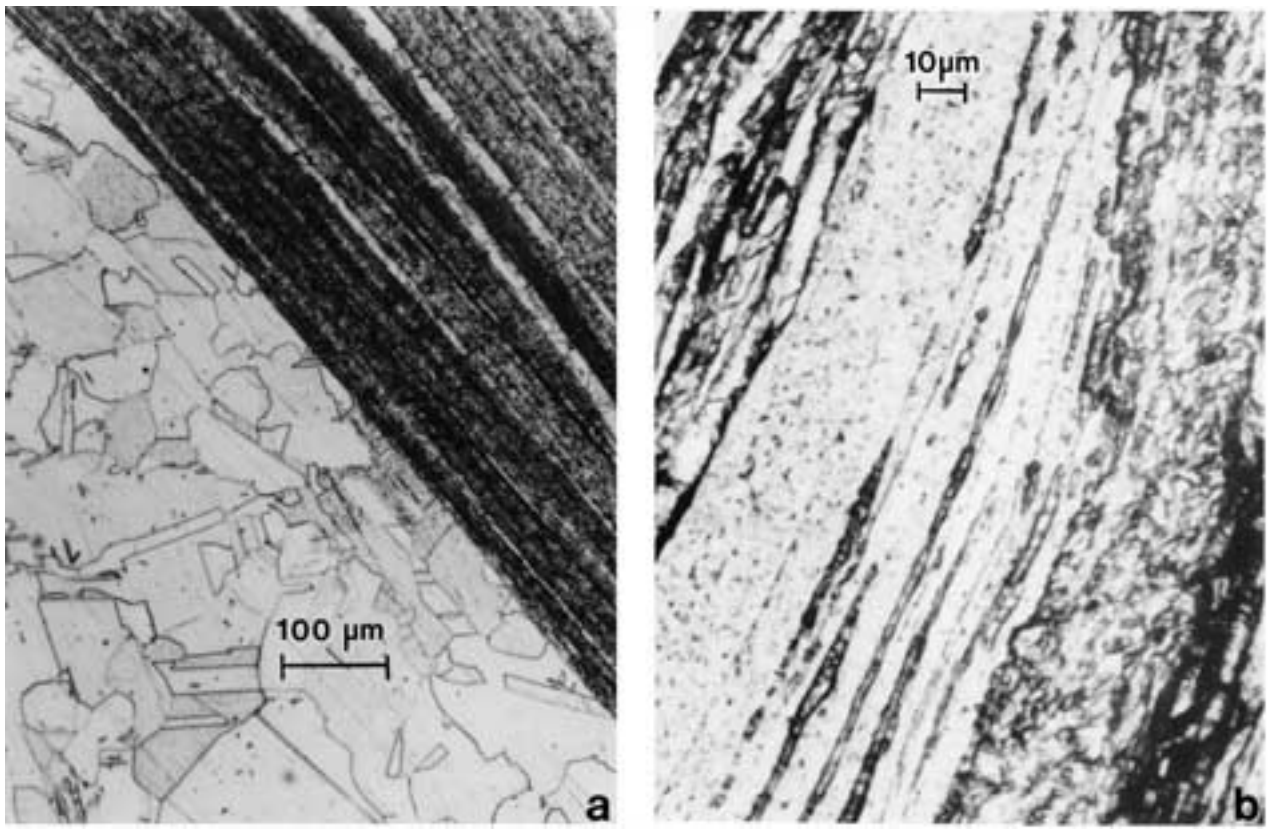

Figure 23 Summary and comparison of solid-state flow facilitated by DRX in overlapping adiabatic shear bands. (a) Cu FSW zone. (b) [001] W penetrator head flow. (c) Flow of Cu crater rim. (d) FSW zone in 6061 Al with Cu particles (arrows). (*Continued.*)

rotational phenomena. Rotational and other related phenomena may also contribute to grain growth which may also result in lower misorientations and reduced interfacial area.

Using molecular dynamics simulations of grain growth in nanocrystalline fcc metals, Haslam *et al.* [21] recently observed that grain boundary migration is triggered preferentially on the long sides of elongated

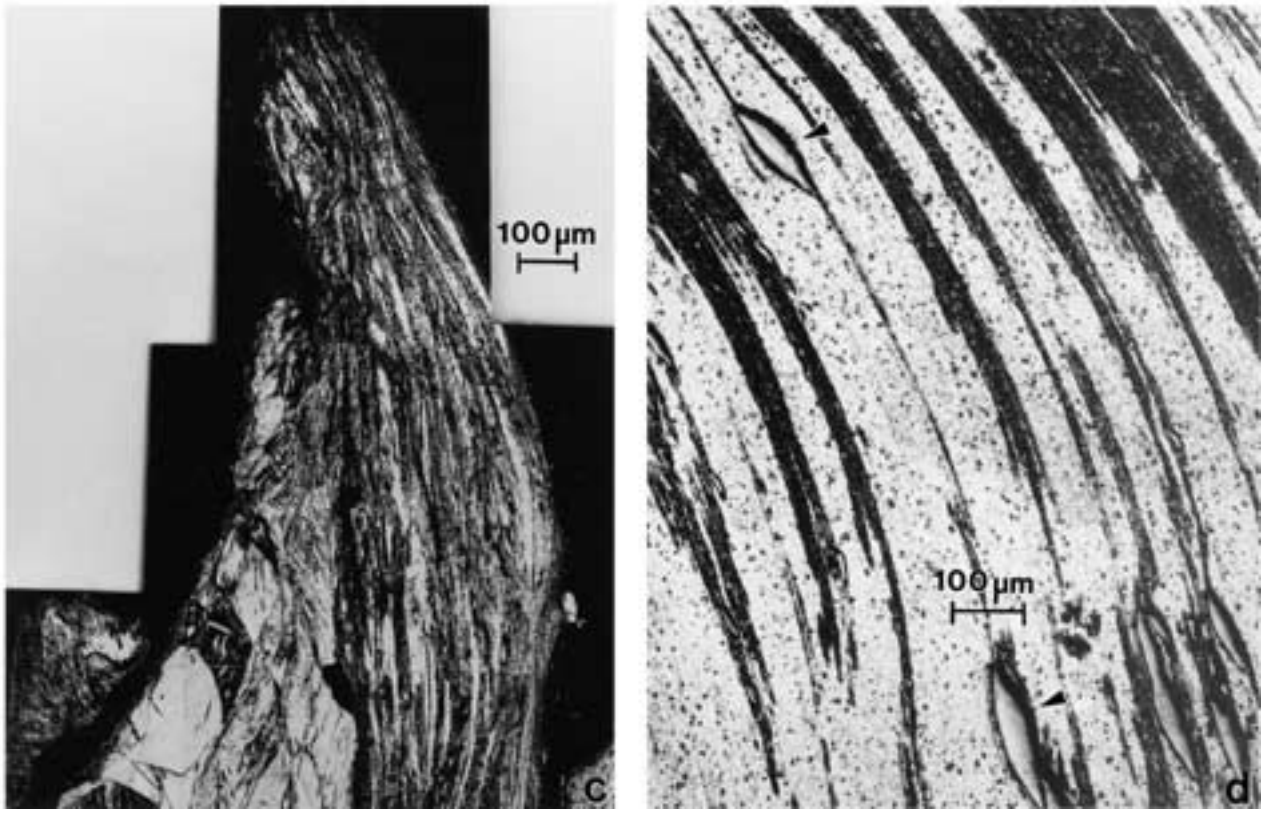

Figure 23 (*Continued*.)

grains; thus tending to restore the isotropic grain shape. Grain growth by curvature-driven GB migration was observed to be dominated by the high-angle (high-energy) GB's in the system; i.e., higher-energy GB's have higher mobility. In effect, grain growth is observed to be driven in part by the conversion of high-angle into low-angle GB's (and consistent with the second law of thermodynamics). Grain rotation can also play a role in lowering the excess energy stored in high-angle GB's, especially for very small (nanocrystalline) grain structures because these small grains are more easily rotated by resolved torques [14]. In pure material, grain rotations only contribute to grain growth if the grain size is of nanometer dimensions. More generally, rotations are activated only for the smallest grains in any grain size distribution, and are also more likely in a polycrystal containing a large fraction of low-angle GB's (or GB's which are vicinals of "special" low-angle GB's) than in a polycrystalline "regime" containing mostly high-angle GB's. This is because high-angle GB's migrate while low-angle GB's rotate. By eliminating grain boundaries between neighboring grains, such rotations lead to grain coalescence and the formation of elongated grains. Therefore, it is not surprising to observe very elongated grains and even equiaxed grains following severe deformation which exhibit very low angles of misorientation. These microstructures are not recovery microstructures as are popularly deduced as a consequence of the low misorientation angles, but are a thermodynamically more stable microstructural evolution associated with recrystallization and grain growth accommodating the SPD process.

While Hines and Vecchio [12] have demonstrated the facility of DRX in the high-strain rate deformation of copper, Vecchio *et al.* [22] have also recently demonstrated that recovery misrostructures can also facilitate SPD in systems like tantalum. While the specific microstructural issues involved in solid-state flow for SPD are complex, the basic mechanism involves fundamental shear band phenomena as summarized in the comparisons of Fig. 23. This figure also summarizes the illustrations and examples provided in this paper and many other examples involving shear bands, localized flow regimes, etc. [23]. Regardless of the specific mechanism or sequence of grain refinement, shear localization, shear band overlap or shear band intercalation contributing to SPD (and especially high-strain-rate deformation), the refined microstructure accommodates large strains by either continuous or discontinuous solid-state flow.

Acknowledgments

This research was supported in part by a Defense Augmentation Award (DAAG55-97-1-0238) for Science and Engineering Training through the U.S. Army Research Office (ARO), the U.S. Army Research Laboratory, Aberdeen Proving Grounds, MD (DAAD-17-01-P-0359), and NASA Johnson Space Center Grant NAG9-1100. We thank Lee Magness at ARL for his cooperative interactions along with Fred Hörz at NASA-JSC. Thanks also to David Brown for his technical help in various aspects of friction-stir welding.

References

1. L. Z. VALIEV, *Ann. Chim.-Mater. Sci.* **21** (1996) 369.
2. L. E. MURR, C.-S. NIOU, E. FERREYRA, E. P. GARCIA, G. LIU, F. HÖRZ and R. P. BERNHARD, *J. Mater. Sci.* **32** (1997) 3143.

3. L. E. MURR, S. A. QUINONES, E. FERREYRA, A. AYALA, O. L. VALERIO, F. HÖRZ and R. P. BERNHARD, *Mater. Sci. Engng.* A **256** (1998) 166.
4. C. KENNEDY and L. E. MURR, *Mater. Sci. Engng.* A **320** (2002) 131.
5. S. PAPPU, C. KENNEDY, L. E. MURR, L. S. MAGNESS and D. KAPOOR, *Mater. Sci. Engng.* A **262** (1999) 115.
6. G. B. OLSON and J. F. MESCALL, in "Shock Waves and High-Strain-Rate Phenomena in Metals," edited by M. A. Meyers and L. E. Murr (Plenum Press, New York, 1981) p. 221.
7. S. L. SEMIATIN, G. D. LAHOTI and S. I. OH, in "Material Behavior Under High Stress and Ultra-high Loading Rates," edited by J. Mescall and V. Weiss (Plenum Press, New York, 1983) p. 119.
8. L. E. MURR, R. D. FLORES, O. V. FLORES, J. C. McCLURE, G. LIU and D. BROWN, *Mater. Res. Innovations* **1** (1998) 211.
9. YING LI, L. E. MURR and J. C. McCLURE, *Mater. Sci. Engng.* A **271** (1999) 213.
10. S. BENEVIDES, YING LI and L. E. MURR, in "Ultra-Fine Grained Materials," edited by R. S. Misra, S. L. Semiatin, C. Suryanarayana, N. N. Thadhani and T. C. Lowe (TMS, Warrendale, PA, 2000) p. 155.
11. A. MARCHAND and J. DUFFY, *J. Mech. Phys. Solids* **36** (1988) 251.
12. J. A. HINES and K. S. VECCHIO, in "Metallurgical and Materials Applications of Shock-Wave and High-Strain-Rate Phenomena," edited by L. E. Murr, K. P. Staudhammer and M. A. Meyers (Elsevier Science, B.V., Amsterdam, 1995) p. 421.
13. T. W. WRIGHT, in "Fundamental Issues and Applications of Shock-Wave and High-Strain-Rate Phenomena," edited by P. Staudhammer, L. E. Murr and M. A. Meyers (Elsevier Science, Amsterdam, 2001) p. 457.
14. L. E. MURR, "Interfacial Phenomena in Metals and Alloys" (Addison-Wesley, Reading, MA, 1975). Reprinted 1990 by Techbooks, Herndon, VA.
15. J. C. M. LI, *J. Appl. Phys.* **32** (1961) 525.
16. J. J. GILMAN, *Phil. Mag.* A **76**(2) (1997) 329.
17. J. C. M. LI, *JOM* **53**(11) (2001) abstract. Also in TMS Meeting Directory (2002) p. 83.
18. L. E. MURR, Y. LI, R. D. FLORES, E. A. TRILLO and J. C. McCLURE, *Mater. Res. Innovations* **2**(3) (1998) 150.
19. L. E. MURR, G. SHARMA, F. CONTRERAS, M. GUERRA, S. H. KAZI, M. SIDDIQUE, R. D. FLORES, D. J. SHINDO, K. F. SOTO, E. A. TRILLO, C. SCHMIDT and J. C. McCLURE, in "Aluminum 2001—Proc. TMS 2001 Aluminum Automotive and Joining Sessions," edited by S. K. Das, J. G. Kaufman and T. J. Lienert (TMS, Warrendale, PA, 2001) p. 197.
20. H. KAZI and L. E. MURR, in "Friction Stir Joining and Processing," edited by K. Jata, M. Mahoney, S. L. Semiatin, R. Mishra and D. F. Field (TMS, Warrendale, PA, 2001) p. 105.
21. A. J. HASLAM, S. R. PHILLPOT, D. WOLF, D. MOLDOVAN and H. GLEITER, *Mater. Sci. Engng.* A **318** (2001) 293.
22. M. T. PEREZ-PRADO, J. H. HINES and K. S. VECCHIO, *Acta Mater.* **49** (2001) 2905.
23. L. J. KESKES, in "Fundamental Issues and Applications of Shock-Wave and High-Strain-Rate Phenomena," edited by K. P. Staudhammer, L. E. Murr and M. A. Meyers (Elsevier Science, B.V., Amsterdam, 2001) p. 259.

Received 24 January
and accepted 25 April 2002